The International Journal of Advanced Manufacturing Technology
https://doi.org/10.1007/s00170-026-18155-w

ORIGINAL ARTICLE

Low-pressure forming and reactive sintering for the synthesis of equimolar CoCrFeNi bulk alloys

Magdalena Lassinantti Gualtieri[1] · **Elena Colombini**[1] · **Enrico Paradisi**[1] · **Cecilia Mortalò**[2] · **Paolo Veronesi**[1]

Received: 27 September 2025 / Accepted: 13 April 2026

Abstract

This work presents a binder-aided process that enables uniaxial pressing of fine metal powders in the low-pressure regime of the compressibility curve, yielding consolidated alloys after debinding and pressureless sintering. Unlike traditional powder metallurgy, where applied loads exceed the powder yield stress, the proposed method relies on powder rearrangement and cohesion made possible by a lubricant/binder. Equimolar CoCrFeNi alloys are synthesized using this strategy with stearic acid serving as lubricant/binder. Reactive sintering is carried out at 1200 °C, resulting in the formation of a single-phase face-centered cubic (FCC) CoCrFeNi alloy. Particular attention is given to the lubricant/binder admixing procedure (solvent-aided or mechanical mixing) and its influence on powder characteristics, compaction behavior, and the resulting microstructure. Lubricant distribution is evaluated by laser diffraction and elemental mapping, while density and porosity are evaluated using established methods and phase composition is determined by X-ray diffraction. It is shown that reactive fine powders admixed with stearic acid using a solvent-aided route lead to a more uniform additive distribution and more effective debinding compared to mechanical mixing, while resulting in lower densification, with relative densities up to ~ 0.9. The proposed approach is particularly relevant for applications such as sputtering targets for physical vapor deposition (PVD), where full densification is not critical for their performance.

Keywords Multi-principal element alloy · Medium entropy alloy · Powder metallurgy · Admixed lubricant/binder · Powder properties

1 Introduction

Multi-principal element alloys (MPEAs), also called complex concentrated alloys (CCAs), cover the inner regions of multi-principal element phase diagrams [1]. High entropy alloys (HEAs) can be considered a subgroup of MPEAs and tend to form simple solid solutions with high (face-centered cubic or body-centered cubic) or medium–high symmetry (hexagonal close-packed) due to high configurational entropy [2]. In one of the pioneering works, compositional limits were defined to fully utilize the stabilizing effect of high mixing entropy, namely more than five elements with concentrations between 5 and 35 at% [2]. The stability of simple solid solutions was experimentally verified for a wide range of alloy compositions synthesized by different routes (arc-melting and casting/splat quenching, as well as thin-film deposition by RF sputtering using an as-cast HEA as target) and subsequently subjected to prolonged annealing [2]. Several notable properties emerged, such as high hardness, high strength, extended ductility at high temperatures and resistance to annealing softening [2]. It was concluded that this new concept had the potential to inspire the development of new materials, theories, and applications, a prediction that was later confirmed by extensive research [1, 3, 4]. In addition to HEAs, medium-entropy alloys (MEAs), typically consisting of three or four principal elements, may likewise form stable simple solid solutions, as their configurational entropy remains sufficiently high to contribute significantly to phase stabilization [4].

✉ Magdalena Lassinantti Gualtieri
Magdalena.gualtieri@unimore.it

[1] Department of Engineering "Enzo Ferrari", University of Modena and Reggio Emilia, Via P. Vivarelli 10/1, 41125 Modena, Italy

[2] National Research Council of Italy-CNR, Institute of Condensed Matter Chemistry and Technologies for Energy–ICMATE, Corso Stati Uniti, 4, 35127 Padova, Italy

Among these multi-principal element systems, face-centered cubic (FCC) solid solutions based on 3 d transition metals are the most extensively investigated, the most prominent example being the equimolar CoCrFeNiMn (Cantor alloy) and its medium-entropy derivatives such as CoCrFeNi [4]. This last quaternary composition possesses interesting mechanical and functional properties [5, 6].

In addition, the FCC phase is stable over a wide temperature range and is thus a suitable matrix for precipitation strengthening phases [7, 8] and ceramic phases inhibiting grain growth [9].

Liquid state processing, like casting, is a common route for producing bulk MPEAs but may be challenging in systems containing elements with widely different melting temperatures with a pronounced tendency to favor microsegregation and volatilization of some of the components [10]. Metal additive manufacturing technologies such as powder bed fusion, binder jetting and metal extrusion are rapidly evolving due to their potential to produce components with high flexibility when it comes to shape and microstructure design [11]. Powder metallurgy (PM) represents an attractive alternative processing route, as it involves sintering, i.e., a heat treatment performed below the melting point of the principal element(s), thereby limiting or avoiding the formation of a liquid phase [12]. The most common PM routes for MPEA synthesis include press-sinter [13, 14], metal injection molding (MIM) [15], hot isostatic pressing (HIP) [16] and spark plasma sintering (SPS) [17–19]. Among the available manufacturing routes, uniaxial cold pressing followed by pressureless sintering is especially attractive for components with relatively simple geometries due to its cost-effectiveness, process simplicity, and scalability.

Surface coatings are widely used to enhance the functional and mechanical performance of engineering components. In this context, HEA coatings have attracted increasing attention due to their outstanding properties in demanding environments, including high hardness, strength, fracture toughness, and resistance to oxidation and corrosion, as well as interesting magnetic and electrical characteristics [20, 21]. In particular, physical vapor deposition (PVD) techniques such as magnetron sputtering (MS) have gained increasing attention for the deposition of MPEA coatings, as film properties can be tailored through both target composition and processing parameters [22]. MPEA sputtering is typically performed by co-sputtering from multiple targets or by sputtering from a single prealloyed target. The use of multiple elemental targets to deposit multicomponent films with controlled composition can be technically complex, particularly when uniform coatings are required on substrates with intricate geometries. As a result, prealloyed targets are often preferred for such applications. Previous work has demonstrated that prealloyed HEA targets produced via simple press–sinter powder metallurgy route can be successfully employed for magnetron sputtering, yielding stable deposition conditions and homogeneous coatings [13]. In that study, sputtering targets with a relative density of approximately 0.79 were successfully employed, indicating that, in the context of PVD applications, full densification is not a strict requirement. Accordingly, the development of simplified and scalable powder metallurgy routes for the fabrication of such targets is of particular interest. Despite its advantages, the application of conventional press–sinter processing to MPEAs produced from mixed elemental powders remains challenging. These powders typically exhibit low compactability due to irregular particle morphology, work hardening during mixing, and solid solution strengthening effects. Hence, high compaction pressures are generally required to achieve sufficient green strength and densification, which may exceed the capabilities of standard laboratory equipment and limit process scalability. This issue is particularly critical for exploratory alloy development, where flexible and accessible processing routes are needed.

In its conventional form, the press-sinter route relies on plastic deformation and cold welding between particles during compaction to achieve high green density and sufficient mechanical strength to withstand ejection stresses. The process efficiency is highly dependent on frictional forces acting during pressing and ultimately affecting the ratio of transmitted load to applied load. Frictional forces are generally attenuated by using lubricants, applied on the die or admixed in the powder or both [23, 24]. Studies show that the effect of internal lubrication depends on the compaction regime. In the early stage of compaction, where particle rearrangement dominates, admixed lubricants reduce interparticle friction and may promote densification better than die lubrication [23, 24]. However, in the plastic deformation regime, increasing internal lubricant content may inhibit cold welding between particles by limiting direct metal–metal contact and occupying volume within the compact. The cross-point between these regimes, the so-called transition pressure, decreases with increasing lubricant content [24]. For example, for water atomized iron powder lubricated with zinc stearate, the transition pressure was reported to decrease from approximately 450 MPa at 1 wt% to about 200 MPa at 3 wt% lubricant [24]. In addition to facilitating powder compaction, lubricants play a crucial role during the ejection of the green compact from the die, which is typically achieved by applying pressure through the lower punch. By reducing friction between the compact and the die wall, lubricants minimize the risk of cracking and mechanical damage during removal. Regarding ejection stresses, internal lubrication appears to be preferable to die-lubrification and a steady decrease was observed with lubricant concentrations up to 4 wt% [24]. Conventional press–sinter processing therefore employs low lubricant additions (typically <1 wt%) as a compromise between improved ejection behavior and preservation of deformation-driven densification. However, this limitation is intrinsically linked to the expectation that close-to-final densification must occur during compaction. If densification is instead primarily achieved during sintering, for example through the use of highly reactive fine powders, operation in the rearrangement regime can be not only viable but advantageous. In such a case, high green density during compaction is no longer the primary objective, and larger amounts of organic additive may be tolerated. At elevated contents, the organic phase can simultaneously reduce interparticle and die-wall friction during compaction and provide cohesive forces that stabilize the green compact, thereby acting as both lubricant and binder. Considering cost and equipment availability, cold forming by uniaxial pressing at modest loads for successive sintering yielding MPEAs is highly attractive, either starting from mixtures of fine elemental powders that alloys during sinter through reactive sintering [13] or carefully selecting the finer part of the particle size distribution of prealloyed powders that are intrinsically hard and thus less attractive for conventional press-sinter processing [25, 26].

This work focuses on the development of an alternative press–sinter route tailored for fine, reactive metal powders with low compactability, which in conventional uniaxial pressing require high forming pressures to achieve sufficient green strength and withstand ejection stresses. The proposed approach explores the low-pressure region of the compressibility curve, enabled by the use of stearic acid as a combined lubricant and binder, reducing interparticle friction while providing sufficient cohesion for green body stability. In this way, forming is decoupled from plastic deformation and cold welding between particles, which are typically required in conventional press–sinter processing. The feasibility of operating in the rearrangement-dominated regime is supported by the high reactivity of fine elemental powders, allowing densification and alloy formation to occur primarily during sintering [13, 15]. This approach also eliminates the need for prealloying techniques such as atomization or mechanical alloying. For process development, the equimolar CoCrFeNi system was selected as a representative MPEA with high technological relevance. Particular attention is given to the lubricant/binder admixing route, comparing mechanical mixing [27–32] and solvent-aided approaches [24, 33–35], and their influence on powder characteristics, compaction behavior, and the resulting microstructure after sintering.

The aim of this work is therefore to evaluate the feasibility of this alternative processing strategy and to identify the associated process–structure relationships, including the trade-offs between densification, powder characteristics, and additive-related effects. The results show that low-pressure forming combined with reactive sintering enables the formation of FCC CoCrFeNi alloys under the investigated conditions, while highlighting the inherent trade-offs between densification and process control.

2 Experimental

2.1 Powder preparation and processing

The purity and suppliers of the elemental powders used for the preparation of equimolar mixtures of CoCrFeNi were as follows: Fe 97% from Aldrich; Ni, Co and Cr $>$99% from Alfa Aesar (SEM images shown in Figure S1). Mixing of the carefully weighted powder blend was performed by ball milling using a PM100 from Retsch. The 250 mL steel jar was charged with 500 g of steel grinding balls of various diameters (d) together with 50 g of metal powder mixture (i.e. ball-powder ratio of 10). Specifically, the grinding balls used were the following: 22 with $d=15$ mm; 32 with $d=10$ mm; 30 with $d=7$ mm; 58 with $d=5$ mm. Intermittent grinding with an effective time of 1 h at 250 rpm was performed (10 min of pause, 15 min of grinding). All operations during this stage, including powder weighting as well as charging and discharging of the jar, were done in a glovebox maintaining an inert (Ar) and anhydrous atmosphere.

Following mechanical mixing, the powder was admixed with stearic acid as lubricant/binder following two different routes; solvent-aided or mechanical mixing. In preliminary experiments, lubricant/binder contents of 0.5, 1, and 3 wt% (relative to the metal powder) were investigated. Based on the real densities of the mixed powder (8.0142 g/cm^3, Section 3.1) and stearic acid (0.845 g/cm^3), these correspond to 4.5, 8.7, and 22.2 vol% stearic acid, respectively. In addition to stearic acid, 0.182 wt% Tween-80 (Sigma-Aldrich) dissolved in ethanol was also added as emulsifier. The two different admixing routes are graphically depicted in Fig. 1. The solvent-aided preparation procedure was as follows: in a first beaker the required amount of stearic acid was dissolved in warm (ca. 40 °C) anhydrous ethanol (Sigma-Aldrich, $>$99.8%). The amount of ethanol was 30 wt% with respect to the metal powder. Complete solubility of stearic acid was obtained (reported solubility of ca. 0.042 mol fraction [36]). In a second beaker, Tween-80 (5.4 mM) was mixed with a second portion of anhydrous ethanol (20 wt% with respect to the powder mixture). In the next step, the Tween-80 solution was added to the metal powder in a

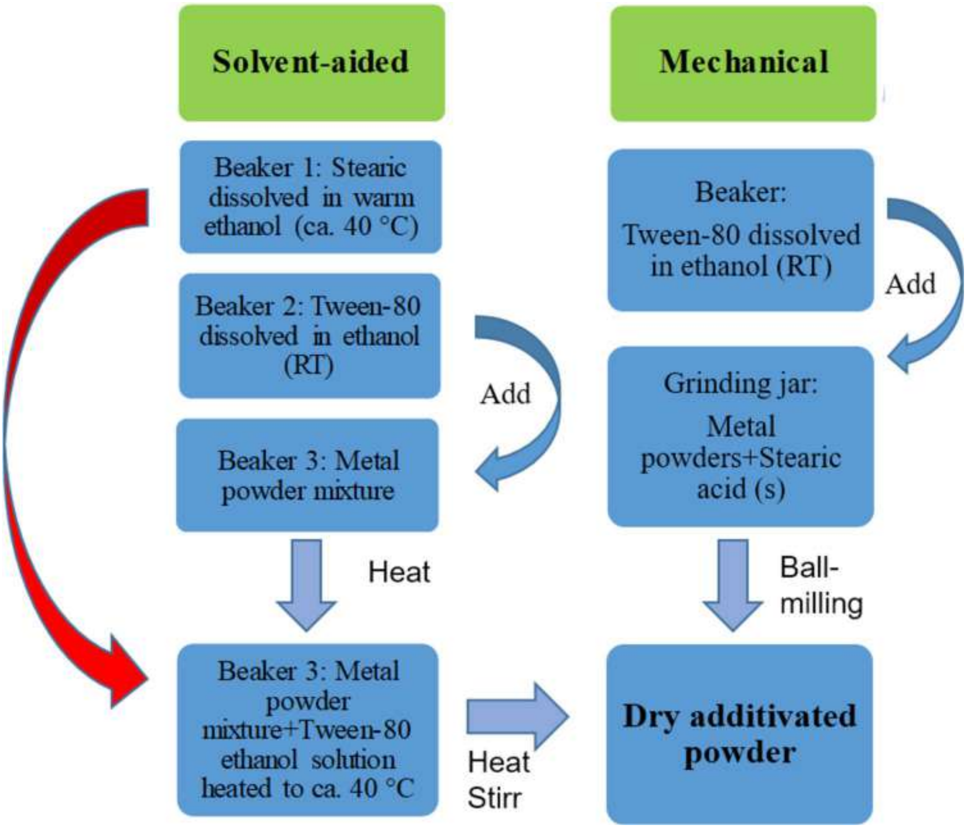

Fig. 1 Schematic description of the two different routes used to prepare metal powders admixed with stearic acid as lubricant/binder for press-sinter processing. Solvent aided: In a first beaker, stearic acid was dissolved in warm ethanol. In a second beaker, a surfactant (Tween-80) was dissolved in ethanol (room temperature, RT). The surfactant solution (beaker 2) was added to a third beaker containing the metal powder and the resulting slurry was heated before adding the lubricant/binder solution (beaker 1). Vigorous stirring under heating resulted in complete evaporation of ethanol and consequently a press-ready dry powder. Mechanical route: The metal powder and stearic acid were placed in a grinding jar together with the surfactant ethanol solution prepared in a separate beaker. The resulting mixture was ball-milled for 1 h at 250 rpm

third beaker. The resulting slurry was then slightly heated before adding the stearic acid solution. This was found to be necessary in order to avoid fast crystallization of stearic acid. The final mixture was vigorously stirred while heated (ca. 40 °C) until complete ethanol evaporation left a homogeneous dry powder. The powder was stored in a glovebox until used. The mechanical admixing route entailed fast ball-milling (same conditions as powder mixing, see above) of the metal powder mixture to which solid stearic acid was added together with the surfactant solution (same proportions as for the solvent-aided preparation procedure). The choice of mixing the powder in a planetary ball mill was motivated by its cohesive nature and the dissimilar nature of the metal powder and the organic additive. Tumbling mixers were judged as unsuitable for the purpose as they are more suitable for powders with high flowability, such as atomized ones.

The admixed powders were uniaxially pressed (70–325 MPa) using a laboratory hydraulic press (Mignon S Nannetti S.r.l.) equipped with a die with a diameter of 25 mm. About 10 g was used for each compact, giving an approximate height of 4 mm. The die was lubricated with an ethanol solution of stearic acid. Relative density as a function of applied load (i.e. compressibility curve) was accomplished in the range 70–325 MPa for the solvent-aided lubricated powder (22.2 vol%). The relative density was calculated from the apparent density of the compacts (from weight and dimensions) and the skeletal density of the base powder measured by He pycnometry.

The organic additive was removed by vacuum treatment using an ISCO NSV 9090 vacuum furnace. The debinding temperature was determined based on simultaneous thermogravimetry–differential thermal analysis of stearic acid (TG–DTA, Netzsch STA 429, heating rate 20 °C min^{-1}) performed under flowing He. The DTA curve exhibits three distinct endothermic events (Fig. 2). The first peak, located

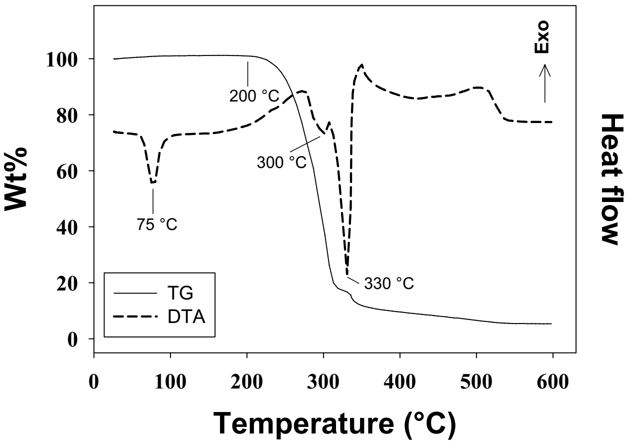

Fig. 2 Results from thermal analysis of the lubricant/binder (stearic acid)

at approximately 75 °C, corresponds to melting and is not accompanied by mass loss, in agreement with literature data [37]. A weak endothermic feature is observed in the range 200–320 °C (maximum at ~ 300 °C) and coincides with the principal mass-loss step (~ 80 wt%). A second, considerably more intense endothermic peak appears between 310 and 350 °C (maximum at ~ 330 °C) but is accompanied by only minor additional weight loss (~ 5.5 wt%). This behavior is consistent with an initial volatilization/evaporation process followed by secondary reactions (pyrolytic decomposition) of the residual fraction [38, 39]. The TG curve shows a slow, continuous mass loss from 350 °C to 540 °C (~ 6.5 wt%), leaving a final residue of ~ 5.5 wt%. Based on the TG–DTA results, 200 °C was selected as the debinding temperature, corresponding to the onset of detectable volatilization and remaining well below the temperature of maximum mass-loss rate. This ensures that binder removal occurs gradually, prior to the rapid mass-loss regime centered near 300 °C, where volatilization becomes intense and secondary pyrolytic reactions begin to contribute. Under vacuum conditions, efficient removal of evolved species further promotes controlled evaporation and limits vapor residence time. Previously reported debinding conditions (e.g., 300 °C for 2 h [40]) are situated within the main mass-loss region identified in the present thermal analysis. Operation within this temperature range corresponds to a regime of rapid volatile release and the onset of thermally activated secondary reactions. In contrast, the lower temperature and extended dwell time employed in the present study promote gradual, transport-assisted binder removal, thereby reducing the likelihood of internal pressure buildup or carbonaceous residue formation during subsequent high-temperature treatment.

Debinded green compacts were sintered in a tube furnace, model RS 80/500/13 from Nabertherm GmBH (Lilienthal, Germany), under constant Ar flux (200 l/h). Prior to sintering, the heating chamber was vacuum conditioned. The thermal cycle included heating up to 1200 °C (350 °C/h) followed by a 4 h long isotherm. The samples were allowed to naturally cool down in the furnace under Ar-flux.

2.2 Characterization methods

The particle size distributions of the base powder and the admixed powders were determined by laser diffraction (Mastersizer 2000, Malvern Instruments Ltd) using distilled water as carrier fluid. The admixed powders were measured both as-is and following removal of the lubricant/binder through washing in acetone (repeated centrifugation and redispersion). Hence, any change in particle size distribution imposed by admixing method could be detected.

Powder flowability was assessed by the Carr index [41] which was calculated according to $100 \times (\rho_t - \rho_a)/\rho_t$ where ρ_t and ρ_a are tapped and apparent density, respectively. The apparent density was determined by gently filling a graduated cylinder with 50 g of powder and reading the volume. The tapped density was calculated from the volume of the same amount of powder following tapping until no further volume change was observed.

Scanning electron microscopy analyses in conjunction with energy dispersive X-ray spectroscopy (SEM–EDS) were performed on powders as well as on the cross-section of pressed compacts and sintered samples. A field emission gun-SEM (FEG-SEM: Nova NanoSEM 450, FEI) was used for this purpose. Powders were sprinkled on carbon adhesive tape and gently tapped to remove excess powder. Green compacts before delubrication/debinding were freshly broken and mounted on aluminum stubs using conductive tape. Sintered samples were metallographically prepared. In particular, the as-sintered samples were cut and hot-mounted in phenol resin. Subsequently, sequential grinding up to a mesh size of P2000 (SiC abrasive papers) was performed followed by polishing using diamond slurries (3 μm and 1 μm). A final mirror finish was accomplished by polishing with colloidal silica dispersion (ca. 60 nm).

X-ray powder diffraction data were acquired from the as-mixed powder as well as from sintered samples. Data for phase identifications were collected using a third generation Empyrean diffractometer from Malvern-Panalytical. The instrument is equipped with multicore optics (icore and dcore), an X-ray tube (LFF HR, Cu anode) and a 2D solid-state hybrid pixel detector based on Medipix3 technology (PIXcel3D area detector). The icore module, including a Bragg–Brentano HD multilayer mirror (producing monochromatic Kα radiation), was set to the following optics: 0.03 rad soller slit; 1/4° fixed divergence slit; secondary mask of 6 mm. The dcore settings included a 1/4° anti-scatter slit. Data were collected in the 2θ range 10–120°. Data for accurate determination of lattice parameters were collected using a multi-purpose X'Pert PRO diffractometer (PANalytical, Almelo, The Netherlands, Cu Kα). A quasi-parallel incident beam was obtained thanks to the X-ray mirror. The beam width was limited using a beam mask of 20 mm. The diffracted beam passed through a parallel plate collimator, a detector slit, soller slits (0.04 rad) and a flat graphite monochromator before reaching the gas proportional counter. Data were collected in the 2θ-range 10–120° using a step size of 0.02° and 8 s per step. The symmetrical parallel beam configuration results in data with accurate positions of the Bragg reflections [13]. Metallographically prepared surfaces of sintered samples were analyzed. Instead, powder samples were side-loaded in glass sample holders.

Rietveld refinements (GSAS-EXPGUI [42, 43]) were used to determine the phase composition of as-mixed powders and to evaluate the fit of an isotropic FCC structure with data collected from bulk samples. Refined parameters included the reflection profiles (multiterm Simpson's rule integration of the pseudo-Voigt function), the background (shifted Chebyshev function with 3–9 terms depending on the refinement), unit cell parameters and scale factors. The zero shift was only refined for data collected with the Empyrean diffractometer from Malvern-Panalytical. Structure models were taken from the Crystallography Open Database [44].

Skeletal densities were determined by Helium pycnometry (AccuPyc 1330, Micromeritics Inc., USA) for the following samples: pressed compacts following delubrication/debinding (ρ_{sc}); the base powder before and after mixing by ball-milling. The sample volume considered by this technique includes both particles and interparticle voids not accessible to helium (i.e. closed porosity). The closed porosity (CP) of uniaxial pressed powders was calculated according to $CP(\%) = 100 \times (1\text{-}\rho_{sc}/\rho_{sp})$ where ρ_{sc} and ρ_{sp} are the skeletal densities of the delubricated/debinded compact and the mixed base powder, respectively. Instead, the open porosity (OP) was determined in a similar manner using the apparent density of the compact (ρ_{appc}, g/cm^3) ($OP(\%) = 100 \times (1\text{-}\rho_{appc}/\rho_{sc})$). The total porosity (TP) was calculated according $TP(\%) = 100 \times (1\text{-}\rho_{appc/}\rho_{sp})$. The apparent density of the compact was obtained from powder displacement measurements using a GeoPyc 1360 instrument from Micromeritics. This technique records displacement data following consolidation of a highly flowable powder (DryFlo) around the consolidated sample. The recorded volume thus also includes pores and voids not accessible to the powder. The apparent density following sintering was determined by the Archimedes method using water as displacement liquid.

The porosity of consolidated powders ($P_{max} = 325$ MPa) was further characterized by mercury intrusion measurements (MIP) using an Autopore IV 9500 scanning mercury porosimeter (pressure range 0.52–33000 psia). Standard instrumental settings were used for these measurements (equilibrium time of 10 s, contact angle and surface tension of mercury, 130° and 485 dynes/cm, respectively). The samples were extracted from the center of the compact and stored in a glovebox (inert, anhydrous atmosphere) before measurements. The collected raw data (intruded mercury as a function of pressure) were transformed in pore size distributions using the classical Washburn equation [45].

3 Results

3.1 Base powder

The equimolar CoCrFeNi powder was mixed in a planetary ball mill using relatively low speed and short duration (250 rpm and 1 h, respectively). Previous work showed that the adopted mixing process results in cold welding of the constituting elemental powders which counteract segregation during handling and assures a homogeneous distribution of the elements [13]. A potential drawback is work hardening of the powder which decreases compressibility [25]. The crystallographic structures of the elements were preserved and the weight fractions of the individual reactants were close to the nominal ones, as shown by XRPD data and Rietveld refinements reported in Figure S2 and Table S1. Hence, the mechanical action was not intense enough to cause interparticle diffusion and atomic mixing. Some cold welding of the particles took place, leading to coarser particle size distribution with respect to the powder mixture simply blended by hand (Figure S3). According to SEM images, the particles are highly irregular with a large fraction of fine particles (Figure S4), as also observed in the particle size distribution showing that about 30 vol.% of the particles have a smaller size than 10 µm (Figure S3). The highly irregular particles as well as the large amount of fine particles lead to internal friction, mechanical interlocking and cohesive effects [46]. The internal cohesive and frictional effects were further confirmed by a high Carr index (39 ± 3) which indicates a powder with "very very poor flow character" [41].

The real density of the blended and mixed powders, measured by He pycnometry, was 8.1125 ± 0.0095 g/cm^3 and 8.0142 ± 0.0034 g/cm^3, respectively. As the density of the mixed powder was lower than the blended one, some closed porosity was formed during mechanical mixing (ca. 1.2%).

3.2 Optimum concentration of stearic acid-preliminary study using solvent-aided admixing

At the early stages of compaction, powder densification is primarily controlled by particle rearrangement rather than deformation. In this regime, the extent to which particles can rearrange is dictated by the internal friction of the powder. Low internal friction allows particles to slide and rearrange more readily, promoting higher packing efficiency in the early stage of compaction [23, 24]. A preliminary investigation of powder flowability was carried out with varying additions of stearic acid (4.5–22.2 vol%, solvent-aided route) to determine an appropriate lubricant/binder content.

Fig. 3 Carr index for different concentrations of lubricant/binder (solvent-aided) (**a**). The compressibility curve for powder admixed with 22.2 vol% stearic acid (solvent-aided) together with literature data (see text for detailed discussion) (**b**)

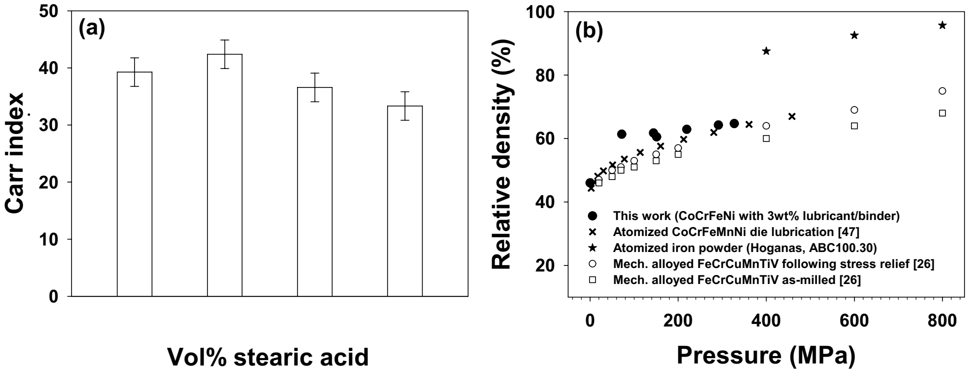

Flowability can be qualitatively assessed through simple techniques such as the Carr index or angle of repose. In this work, the Carr index was chosen to assess powder flowability as a function of added lubricant/binder, see Fig. 3a. As can be observed from the figure, a 22.2 vol% addition of lubricant/binder was needed to obtain a lower Carr index with respect to the base powder considering the experimental error. Hence, this amount of organic additive was chosen for successive experiments.

Figure 3b shows the relative density as a function of load for the mixed powder admixed with 22.2 vol% stearic acid. Data at zero load corresponds to the tap density. Some literature data for different systems are also shown for comparison, with the primary aim of demonstrating the low compactability of the investigated powders and multi-principal alloy powders in general. In particular, atomized CoCrFeMnNi [47] is shown together with a mechanically alloyed FeCrCuMnTiV powder before and after stress relief (1 h 150 °C) [26]. In addition, commercial iron powder (ABC 100.30 from Hoganas, Sweden) is shown to evidence the much higher compactability of powders specifically designed for press-sinter processing. As can be observed from the figure, the compressibility of the mixed CoCrFeNi powder studied here in addition to literature data for pre-alloyed HEA powders (atomized CoCrFeMnNi [47] and mechanically alloyed FeCrCuMnTiV [26]) are considerably worse than commercial press-sinter powders (iron admixed with zinc stearate). This clearly demonstrates the challenge of using uniaxial cold forming for mixed multi-component metal powders. It is interesting to observe that the powder investigated here reaches much higher densities than the prealloyed powders in the low-pressure region where densification by particle rearrangement prevails. This could indeed be the result of better particle packing of the former powder due to a more favorable particle size distribution and/or lower interparticle friction provided by internal lubrication. Another important consideration regarding the selected amount of organic additive is the total pore volume of the pressed compacts. Within the investigated pressure range, the porosity, calculated as $100 \times (1 - \text{relative density})$, does not exceed 35 vol% (see Fig. 3b). Therefore, the chosen binder/lubricant content (22.2 vol%) can be accommodated within the available pore volume and is not expected to be expelled during compaction.

3.3 Admixed powders (22.2 vol% stearic acid)-different admixing routes

The particle size distributions for powders admixed with 22.2 vol% stearic acid were determined by laser diffraction and the results are shown in Fig. 4. For comparison, the results from the base powder are shown together with the admixed powders following washing in acetone by repeated centrifugation and redispersion. Numerical data (D-values) of the particle size distributions are shown in Table S2. Washing was aimed at removing the organic additive

Fig. 4 Particle size distribution of ball-milled equimolar CoCrFeNi (base powder) and the same powder following the addition of stearic acid as lubricant/binder: (**a**) solvent-aided; (**b**) mechanically mixed (ball-milling). Results obtained from the admixed powders following repeated washing in acetone, aimed to remove the fatty acid, are also shown for both admixing methods

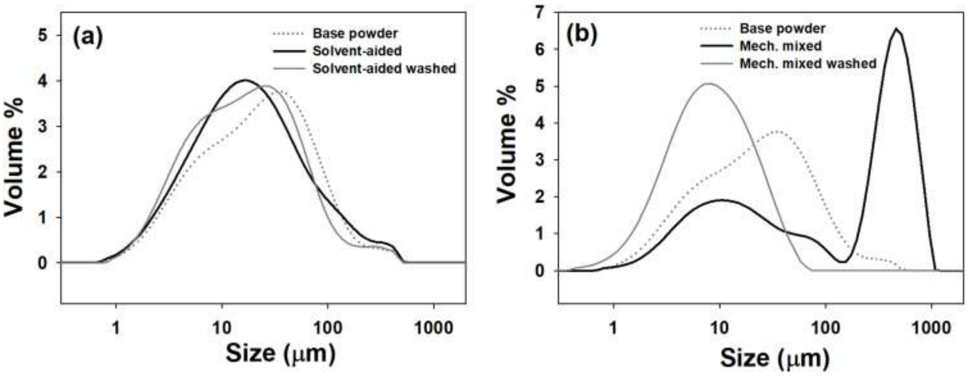

and thus revealing any changes in particle size distribution imposed by the admixing route. The particle size distribution following solvent-aided admixing is slightly finer than that of the base powder (compare base powder and washed admixed powder in Fig. 4a), indicating that stirring during solvent evaporation promotes partial disaggregation of the powder. The admixed powder (i.e., before washing) is only slightly coarser than the washed powder, suggesting that the deposition of the lubricant/binder induces a limited degree of particle association. However, the overall similarity of the distribution curves indicates that this effect does not result in the formation of large agglomerates. Rather, the organic additive is primarily distributed on the surface of the metal particles, consistent with a coating-like mechanism as reported in the literature [31]. Mechanical admixing results in a finer powder (compare base powder and washed admixed powder in Fig. 4b). This indicates particle fracturing favored by the organic compounds acting as process control agents [48]. Another interesting observation is that mechanical admixing results in extensive agglomeration (compare base powder and admixed powder before washing in Fig. 4b). Agglomeration probably occurs as ball-milling results in heat development in the jar that softens the organic additive, making it sticky and binder-like. Although intermittent grinding was used (stop 5 min every 10 min of grinding), the frictional heat slightly increased the temperature of the jar (34 °C measured at the outer surface of the jar directly following mixing). The risk of heat development and unwanted granulation during less energetic mixing like tumbling mixers is lower [49]. Nevertheless, even in this case prolonged mixing may result in the formation of agglomerates. Hence, the process duration should be optimized with respect to powder properties such as flow behavior and density [30, 33].

Backscattered electron (BSE) SEM images and EDS data were collected with the primary aim of revealing the lubricant/binder distribution in the two differently admixed powders. Some representative images are shown in Fig. 5. Instead, EDS elemental maps of the powders are displayed in the supplementary data (Figure S5 and S6 for solvent-aided and mechanically mixed powders) together with EDS area analyses of large agglomerates in the mechanically admixed powder (Figure S7). The carbon elemental map indicates the distribution of the organic additive whereas the oxygen elemental map shows the distribution of both stearic acid and surface oxidized particles. First of all, no free stearic acid particles were found in SEM-analyses. Hence, this lubricant/binder phase was smeared or deposited on the surface of the base powder particles. The main difference between the powders is that the mechanically admixed one appears to contain a larger amount of agglomerates in accordance with laser diffraction data (see Fig. 5). These agglomerates are composed of lubricant/binder intimately mixed with metal particles (see Figure S6 and S7). The organic additive is mainly distinguished at higher magnification by dark contrast and a smeared appearance (see white arrows in Fig. 5 c and f). Higher oxygen content is observed in concomitance with chromium in both powders, indicating some oxidation of this elemental powder (see EDS maps in Figures S6 and S7). However, oxidation was not severe enough to be revealed by XRPD data collected from the admixed CoCrFeNi powders (see supplementary data, Figure S8).

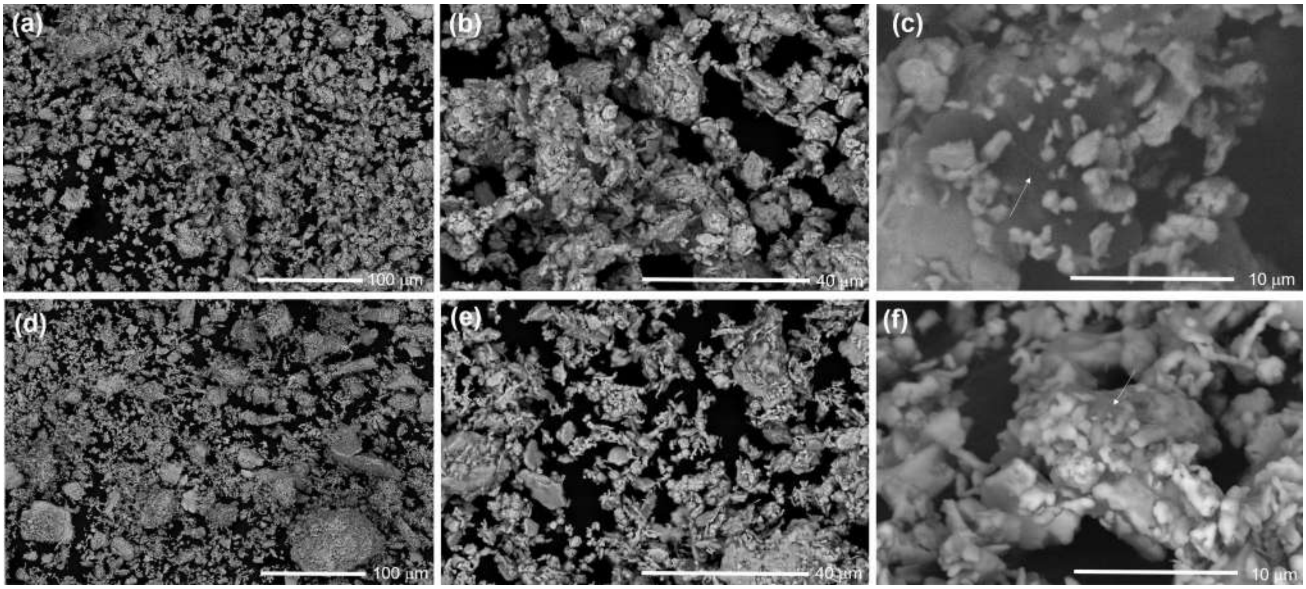

Fig. 5 BSE-SEM images of CoCrFeNi powders admixed with stearic acid by the solvent-aided route (**a**, **b**, **c**) and by mechanical mixing (**d**, **e**, **f**). The arrows in figures (**c**) and (**f**) indicate the lubricant/binder visible at higher magnification

3.4 Pressed compacts (22.2 vol% stearic acid)-different admixing routes

BSE-SEM micrographs were collected from the cross-section of freshly fractured surfaces of green compacts (before delubrication/debinding) to observe the porous structure. Representative data are shown in Fig. 6. Particles coated with stearic acid appear blurry. The width of about 100 voids were measured using ImageJ [50]. The compact obtained from solvent-aided admixed powder had voids in the range 0.14–2.0 µm with a mean void size of 0.5 ± 0.4 µm. Instead, the compact from mechanically admixed powder had voids in the range 0.16–1.8 µm with a mean void size of 0.4 ± 0.3 µm. Of course, this type of evaluation of the porous structure is highly approximate and should only be regarded as indicative. The particle boundaries are still easily identified and no anisotropic arrangement or deformation of particles are evident. This implies that the uniaxial load was not high enough to exceed the yield strength of the powder material.

The lubricant/binder distribution in pressed compacts was evaluated by EDS elemental maps of freshly fractured samples. Figures 7 and 8 show data for compacts obtained from solvent-aided route and mechanical mixing, respectively. As for the powders, the EDS elemental map of carbon is indicative of the lubricant/binder distribution whereas

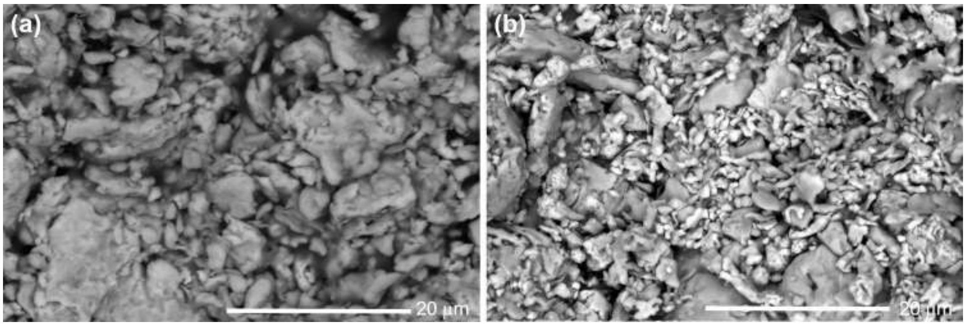

Fig. 6 BSE micrographs of the cross-sections of pressed compacts (pressing direction upwards): (**a**) solvent-aided admixing; (**b**) lubrication by mechanical admixing

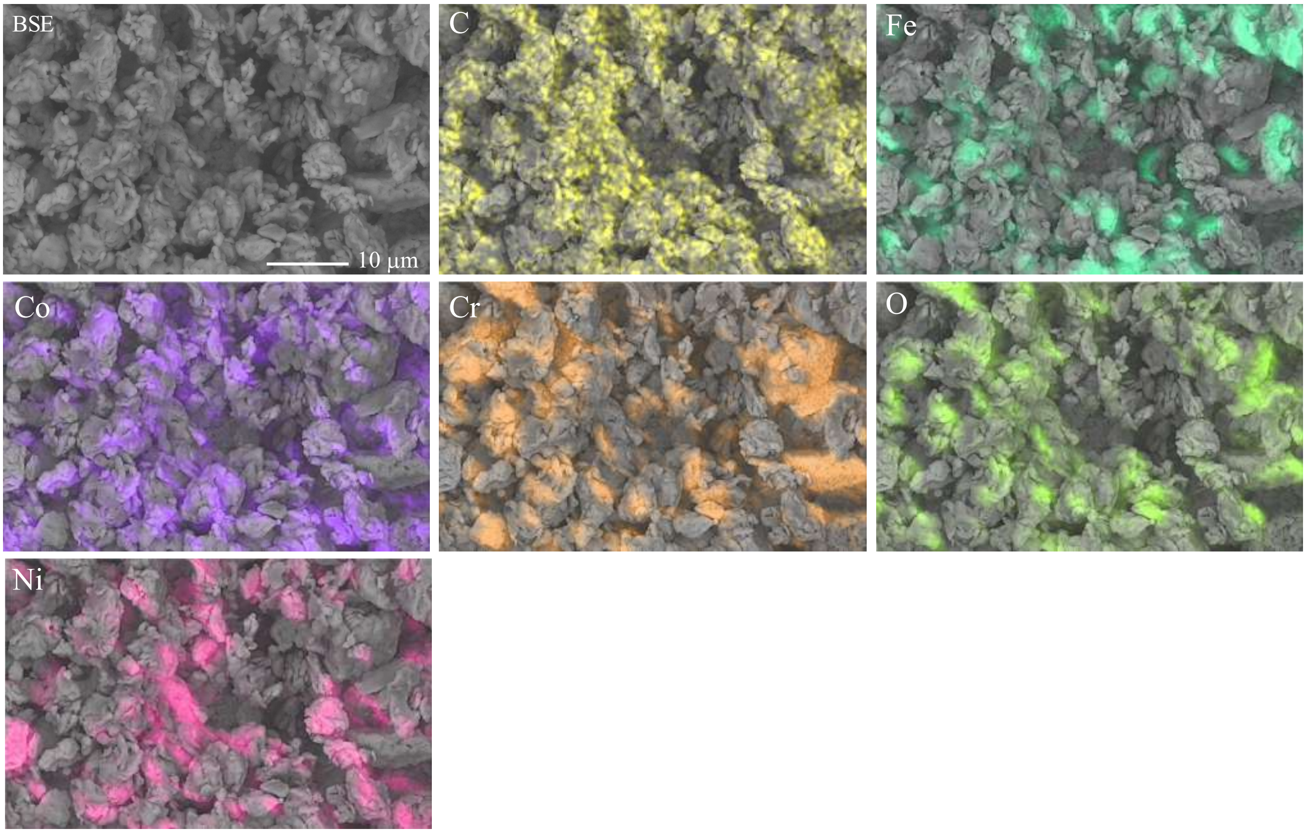

Fig. 7 EDS elemental maps of the powder compact admixed with lubricant/binder (stearic acid) by the solvent-aided route (cross-view with the pressing direction upwards). The lubricant/binder appears dark in the BSE image

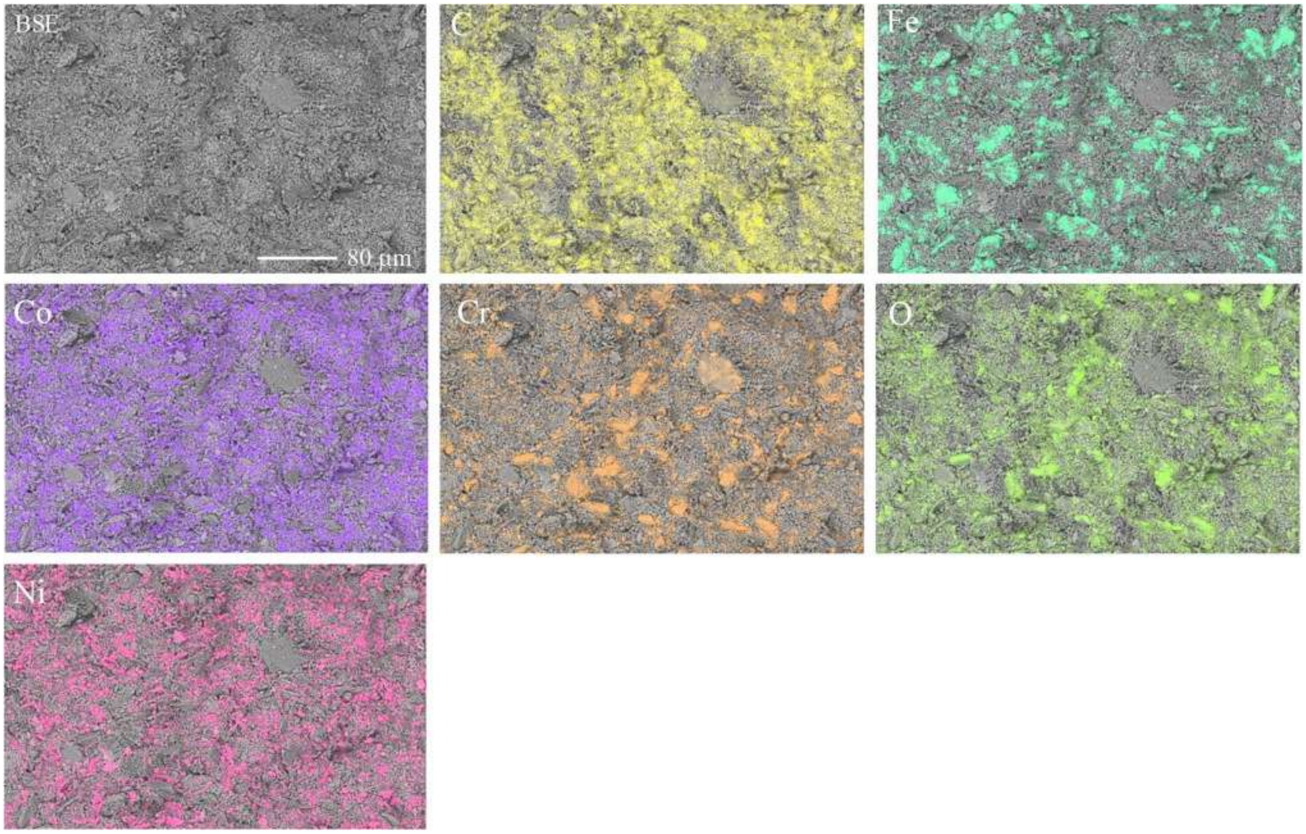

Fig. 8 EDS elemental maps of the mechanically admixed powder following uniaxial pressing

Table 1 Densities and porosities of green (after removal of lubricant/binder by vacuum evaporation) compacts prepared from powders to which the lubricant/binder was added either by mechanical mixing or by a solvent-aided route. Closed, open and total porosities (CP, OP and TP, respectively) and relative density (RD) were calculated from the apparent density of the compact (ρ_{appc}), the skeletal density of the compact (ρ_{sc}) and the skeletal density of the base powder ($\rho_{sp} = 8.0142 \pm 0.0034$ g/cm^3) Details regarding these calculations are found in the experimental section

P_{max} (MPa)	Admixing	*ρ_{appc} (g·cm^{-3})	**ρ_{sc} (g·cm^{-3})	CP (%)	OP (%)	TP (%)	RD (%)
150	Mechanical	5.28 ± 0.04	N.D	N.D	N.D	34.1 ± 0.3	65.9
	Solvent	4.85 ± 0.04	N.D	N.D	N.D	39.5 ± 0.3	60.5
325	Mechanical	5.88 ± 0.02	7.0576 ± 0.0035	11.96 ± 0.03	16.7 ± 0.2	26.6 ± 0.2	73.4
	Solvent	5.50 ± 0.08	7.0559 ± 0.0033	11.94 ± 0.1	22 ± 1	31.4 ± 0.9	68.6

*From powder displacement (Geopyc 1360, Micromeritics)

**From Helium pycnometry data

the one of oxygen originates from both lubricant/binder and surface oxidation. In fact, oxygen is present in association with chromium (see Figs. 7 and 8). Some signal shadowing is observed, particularly in the EDS maps of the solvent-aided admixed powder compact, as the section was obtained by fracturing leaving an uneven surface. Nevertheless, it appears that the lubricant/binder is more homogeneously distributed in the sample prepared from mechanically admixed powder (compare Fig. 8 with Fig. 7). The explanation for this observation could be that this powder is finer than the one admixed by the solvent-aided route. In fact, laser diffraction data revealed particle comminution during mixing and the formation of large agglomerates composed of intimately mixed particles and lubricant/binder (see Fig. 4). Instead, the solvent-aided route preserved the original particle size distribution and the lubricant/binder was distributed on the surface of the particles. Hence, the coarser powder appears less homogeneous on a macroscopic scale after compaction as the lubricant/binder is found in the interstitial regions of the large particles, closely mixed with the finer particles.

3.5 Green compacts-different admixing routes (22.2 vol% stearic acid)

Table 1 shows the green densities (following vacuum evaporation of the organic additives) of consolidated powders admixed either by mechanical mixing or by a solvent-aided route (22.2 vol% stearic acid). The skeletal density of the compact (ρ_{sc}) as well as the closed, open and total porosities (CP, OP and TP, respectively) are also shown. First of all, higher compaction load results in higher apparent density of the green compact as expected (ρ_{app} in Table 1). Mechanical admixing results in higher values with respect to solvent-aided admixing. This is in contrast to the results obtained by Chen et al. who found higher green densities for solvent-aided admixing for sponge iron powder lubricated with≤1 wt% zinc stearate [31]. The mechanical mixing method used by Chen and co-workers consisted in mild mixing using a double-cone mixer working at 30 rev/min for 60 min. Hence, the particle size distribution following admixing (although not reported) was assumingly not affected on the contrary to mixing by ball-milling used here (see Fig. 4b). Therefore, the inverse relationship between admixing method and green density observed in this study is primarily attributed to differences in particle size distribution (Fig. 4). Additionally, the elevated open porosity in the solvent-aided admixed sample may result from internal porosity within powder aggregates that persists during compaction and is transferred to the green compact.

An important amount of closed porosity was found in both types of samples and the amount was close to identical (i.e. ca. 11%, see Table 1). Instead, the open porosity was higher in the compact obtained from the solvent-aided admixed powder (22% with respect to 16.7% for the compact obtained from the mechanically admixed powder, see Table 1), leading to a higher total porosity (i.e. lower density). The main difference between the two samples thus lies in the amount of pores connected to the outer surface of the compact. A suitable technique to characterize volume and size distribution of open pores is mercury intrusion measurements (MIP). The volume of intruded mercury is recorded as a function of pressure and the collected data is transformed in pore size using the Washburn equation [45] which assumes a network of cylindrical pores connected to sample surface. Increasing the pressure, successively smaller pores are filled with mercury. This assumption fails if larger pores only are accessible through smaller pores. In this case, the volume of the introduced mercury is mistakenly attributed to the smaller pore size, leading to an overestimation of its volume. Nevertheless, MIP gives valuable data on threshold pore sizes and total open porosity. The porous structures of the compacts obtained at the higher forming pressure were investigated by this method. Figure 9a and Fig. 9b show the cumulative pore volume and dV/dlog D (V = volume of intruded mercury) as a function of pore diameter (D).

First of all, the volume of intruded mercury is much lower in the sample prepared from a powder admixed by mechanical mixing (see Fig. 9a). The porosities accessible to mercury intrusion (i.e. open porosity) were calculated to be 16.80% and 20.26% for mechanically and solvent-aided admixing, respectively. These values are in good agreement with data obtained from density measurements (see open porosities reported in Table 1). The MIP data both show a bimodal pore size distribution in the ranges 0.1–0.5 μm and 0.2–1.3 μm for the mechanically mixed powder and powder admixed by the solvent-aided route, respectively. These values are in rather good agreement with those recovered from image analyses of SEM micrographs (see Section 3.4). A narrower distribution and a shift to lower values are observed for the mechanically mixed powder consistent with a higher density and thus better particle packing. Some larger pores are detected in both samples but are not inherent to the porous network formed during powder pressing but are surface voids created during sample preparation, a phenomenon already reported by others [51]. A small fraction of meso- and macropores (10–100 nm) are present in the compact obtained from mechanically admixed powder which was nearly absent in the one obtained from powder admixed by the solvent-aided route. These pores may reflect incomplete evaporation of the organic additive from the main pore population during debinding, giving rise to smaller apparent pore sizes.

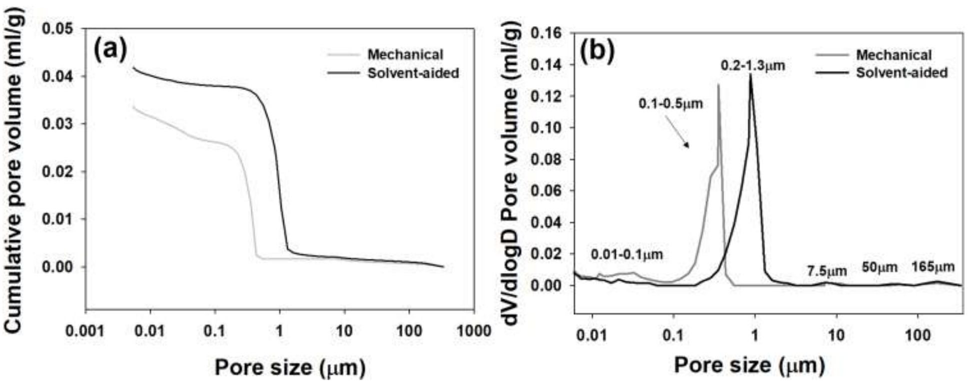

Fig. 9 The cumulative pore volume (**a**) and dV/dlogD (V = volume of intruded mercury) as a function of pore diameter (D) (**b**). Data were collected from admixed powders (either mechanically or by a solvent-aided route) uniaxially pressed at 325 MPa and subsequently subjected to vacuum evaporation of the lubricant/binder

3.6 Sintered compacts-different admixing routes (22.2 vol% stearic acid)

3.6.1 Density

The admixed powders, uniaxially pressed at 325 MPa, were exposed to a mild heat treatment under vacuum to remove the lubricant/binder. Subsequently, reactive sintering was accomplished at 1200 °C for 4 h under Ar-flux. The density of sintered compacts obtained from mechanically admixed powder was 7.51 ± 0.08 g/cm^3. A slightly lower density was found for compacts obtained from the solvent-aided admixed powder (i.e. 7.27 ± 0.04 g/cm^3). The corresponding relative densities were 0.91 ± 0.01 and 0.884 ± 0.005, calculated using the real density of the CoCrFeNi alloy obtained from XRPD data and Rietveld refinements (discussed later, see Sect. 3.6.3). It should however be pointed out that the real density approximated in this way is overestimated as low-density ceramic phases are present (see Sect. 3.6.2). As a consequence, the relative density is higher (i.e. fewer pores are present). The different degree of sintering in the two types of samples is consistent with the observations made for the green compacts, i.e. higher density of the mechanically admixed powder (see Table 1).

3.6.2 Phase composition and distribution by XRPD and SEM–EDS

Figure 10 shows the XRPD pattern collected from the sintered samples (third generation Empyrean diffractometer). Both samples exhibit an alloy phase with FCC symmetry (indexed), in accordance with previous work [13]. Hence, the 4 h long holding time at 1200 °C was enough to form a solid solution MPEA through atomic annealing-induced diffusion between the primary particles. A minor amount of a rhombohedral oxide impurity (pdf nr. 01–084–0314, Cr_2O_3) was identified in both samples, see Fig. 10. This oxide was also found in the CoCrFeNi alloy synthesized by Colombini and co-workers using a similar press-sinter process of mixed powder without internal lubrication [13]. In addition, the sample prepared by mechanical mixing also contained chromium carbide (pdf nr. 00–036–1482, Cr_7C_3). The presence of these secondary phases is better visualized in the inserts depicting a limited 2θ region showing the most intense reflections of the secondary phases (Fig. 10).

SEM–EDS analyses were performed to evaluate the distribution of the ceramic inclusions detected by XRPD. Figures 11 and 12 show BSE-SEM images of sintered samples prepared from powders admixed with stearic acid via the solvent-aided route and mechanical mixing, respectively. The corresponding EDS elemental maps are presented in Figs. 13 and 14. The phase maps allow the secondary phases observed in Figs. 11 and 12 to be correlated with their chemical composition. The press–sinter route involving mechanical admixing results in CoCrFeNi alloys containing inclusions enriched in Cr and C, as well as Cr and O (Fig. 14). In contrast, the sample prepared via solvent-aided admixing exhibits only Cr–O inclusions (Fig. 13). These findings agree with the XRPD analysis (Fig. 10), showing chromium oxide and chromium carbide in the mechanically admixed sample, while only Cr_2O_3 was observed in the solvent-aided counterpart.

Whereas both admixing routes lead to the formation of Cr_2O_3 following sintering, only the sample prepared from mechanical admixing contained Cr_7C_3 (see Fig. 10). The presence of Cr_2O_3 in the sintered samples is consistent with preferential oxidation of Cr in air during handling (see Figs. 7 and 8). In addition, intrinsic oxide layers are

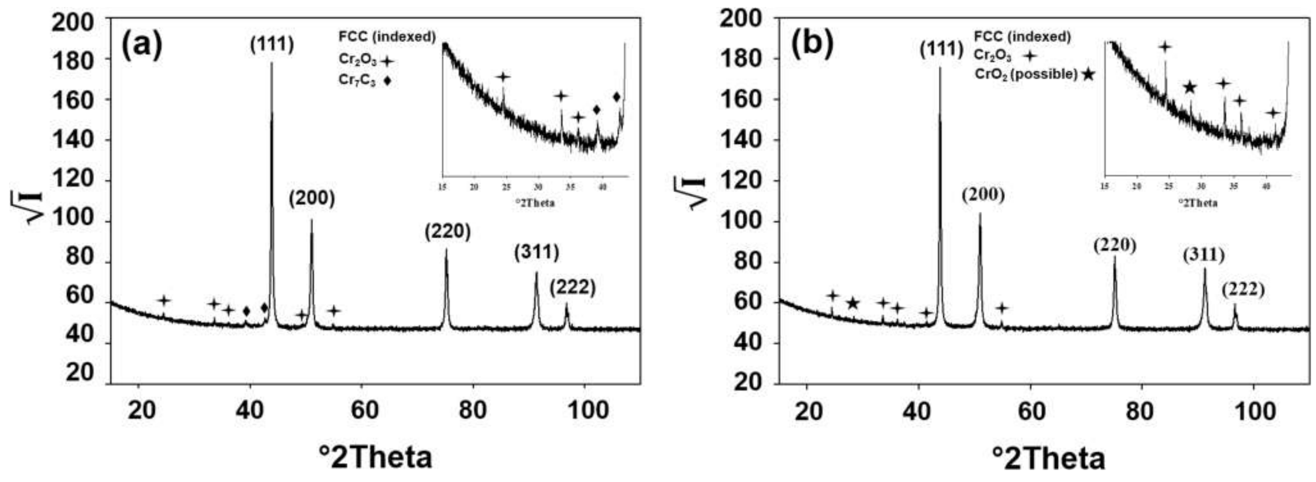

Fig. 10 XRPD data (third generation Empyrean diffractometer) collected from the CoCrFeNi sintered samples prepared from the base powder modified with lubricant/binder by mechanical mixing (**a**) and solvent-aided route (**b**). The inserts show limited 2θ ranges to better accentuate the reflections of secondary phases (Cr_2O_3 and Cr_7C_3)

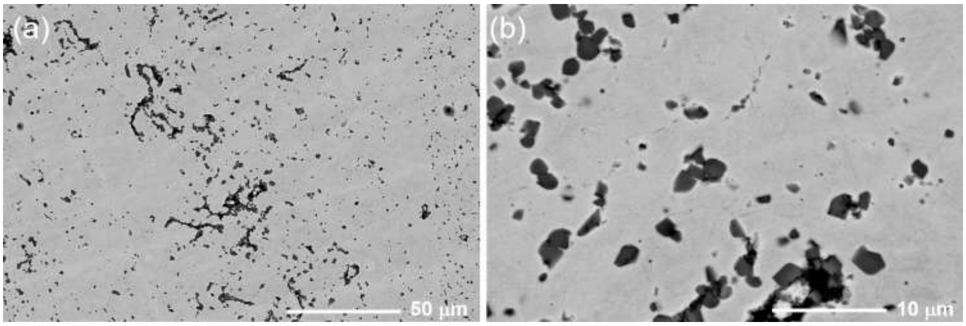

Fig. 11 BSE micrographs of CoCrFeNi alloy obtained by press-sinter of mixed powders admixed with stearic acid using a solvent-aided route. Observe the presence of at least one secondary phase with different contrast

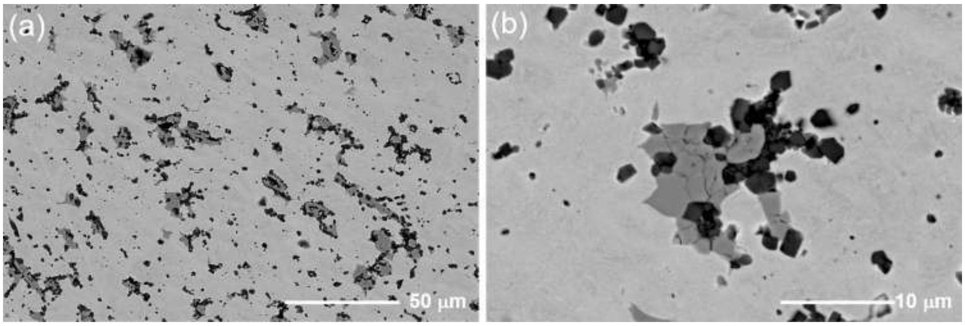

Fig. 12 BSE micrographs of the CoCrFeNi alloy produced by press–sintering of mechanically admixed powders. At least two secondary phases with distinct contrast can be observed in close proximity

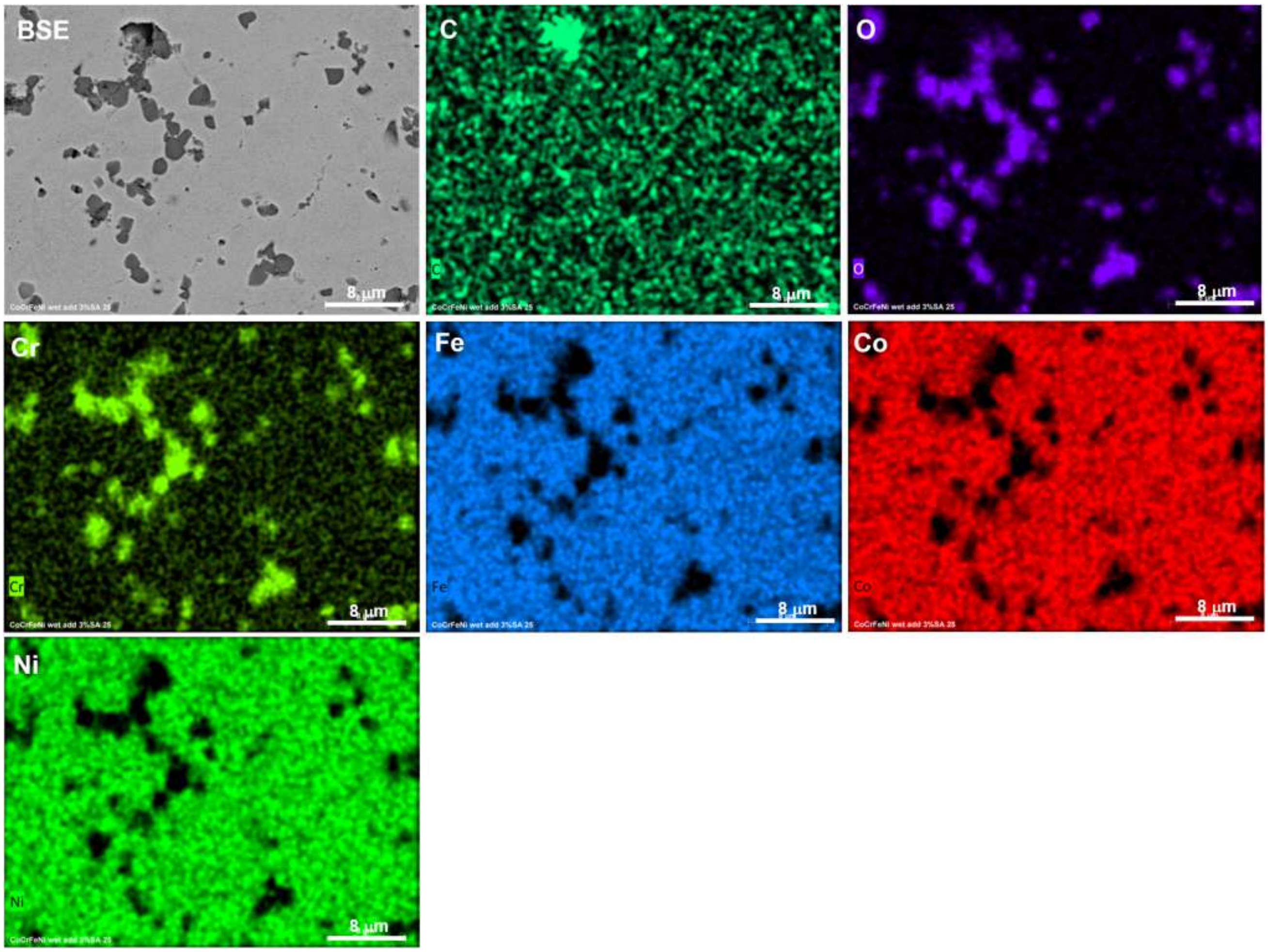

Fig. 13 EDS elemental maps of CoCrFeNi alloy obtained by press-sinter of powders admixed with stearic acid by a solvent-aided route. The secondary phase embedded in the alloy matrix are highlighted. This phase is composed of O and Cr

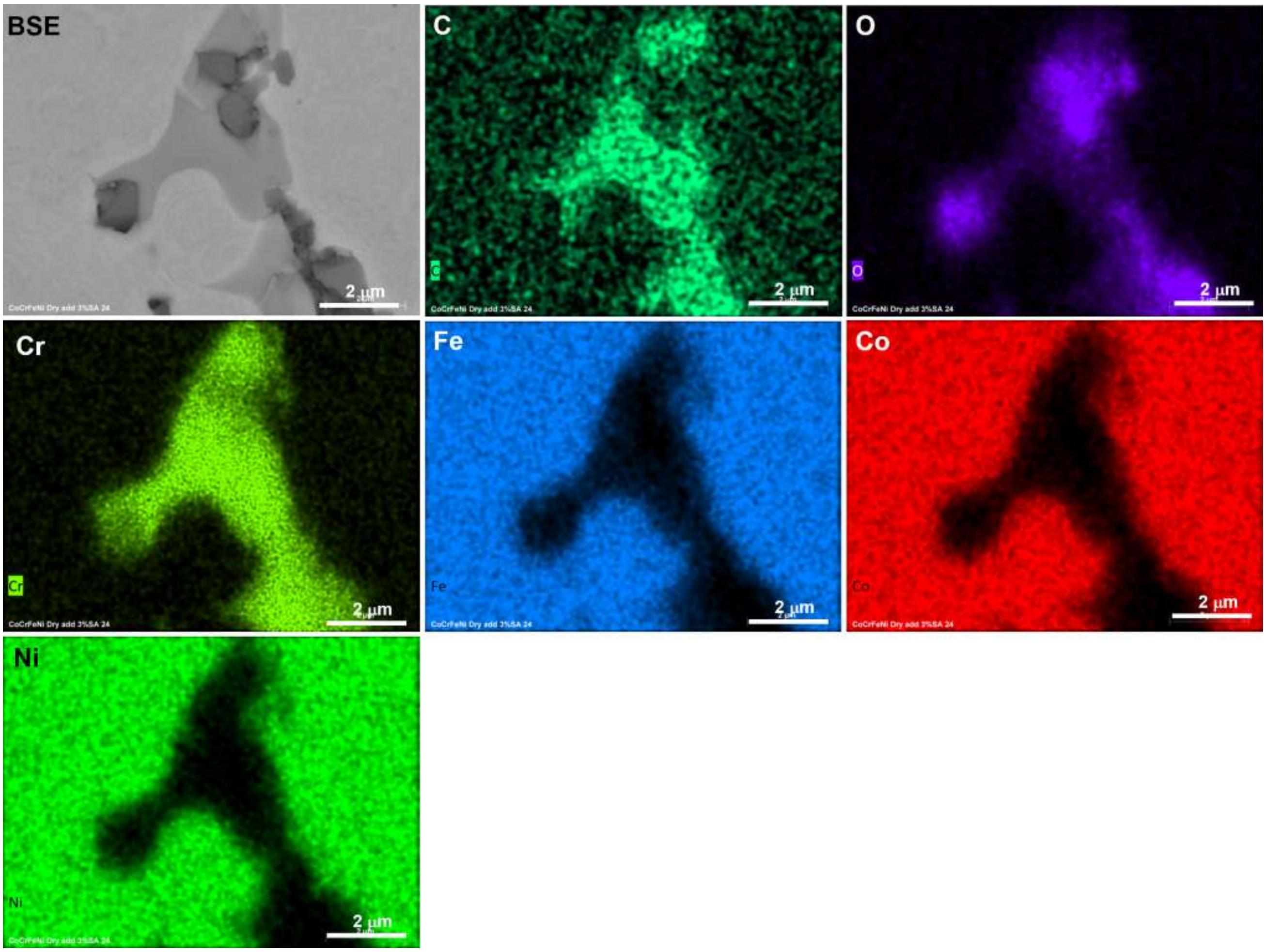

Fig. 14 EDS elemental maps of CoCrFeNi alloy obtained by press-sinter of powders admixed with stearic acid by mechanical mixing. The secondary phases embedded in the alloy matrix are highlighted. The phase with medium contrast is composed of Cr and C whereas the phase with dark contrast is composed of Cr and O

present on commercial powders [52]. During high-temperature treatment, oxide stability follows the thermodynamic hierarchy described by the Ellingham diagram, whereby the less stable oxides of Ni, Co, and Fe may be reduced, while the more stable Cr_2O_3 persists [52]. In contrast, the most likely carbon source responsible for chromium carbide formation in the mechanically admixed system is the organic additive. Two possible mechanisms may be considered. First, mechanical admixing in the presence of organic species may lead to partial carbon incorporation into the alloy during thermal treatment. Second, residual stearic acid may not be fully removed during debinding if its volatilization is hindered by restricted diffusion pathways within the fine pore structure. Regarding the first scenario, crystallization of Cr_7C_3 and Cr_2O_3 during sintering of MPEA powders synthesized by mechanical alloying in the presence of PCAs is commonly reported [53–55]. A possible reason could be decomposition of the PCA during mechanical alloying that ultimately leads to interstitial carbon in the solid solution alloy that during sintering leads to local supersaturation of carbon in chromium-rich regions, promoting precipitation of chromium carbides (e.g. Cr_7C_3) [55]. In the mechanical mixing procedure performed here, much less energy is embedded in the process (250 rpm for 1 h with respect to e.g. 450 rpm for 10 h in [55]) and the crystallographic nature of the constituting elements is preserved (Figure S8). Therefore, little or no structural carbon is expected to be incorporated in the metallic phases. The second scenario, namely incomplete removal of stearic acid during the prolonged vacuum treatment, is more probable and indirectly supported by MIP data (see MIP data in Fig. 9). If residual stearic acid remains after debinding at relatively low temperature, it is likely present predominantly as solidified stearic acid rather than as extensively degraded carbonaceous material. During subsequent high-temperature sintering in an inert atmosphere, this residual organic phase can undergo thermal decomposition, generating smaller gaseous species such as H_2, CH_4, CO, CO_2, H_2O, and light hydrocarbons

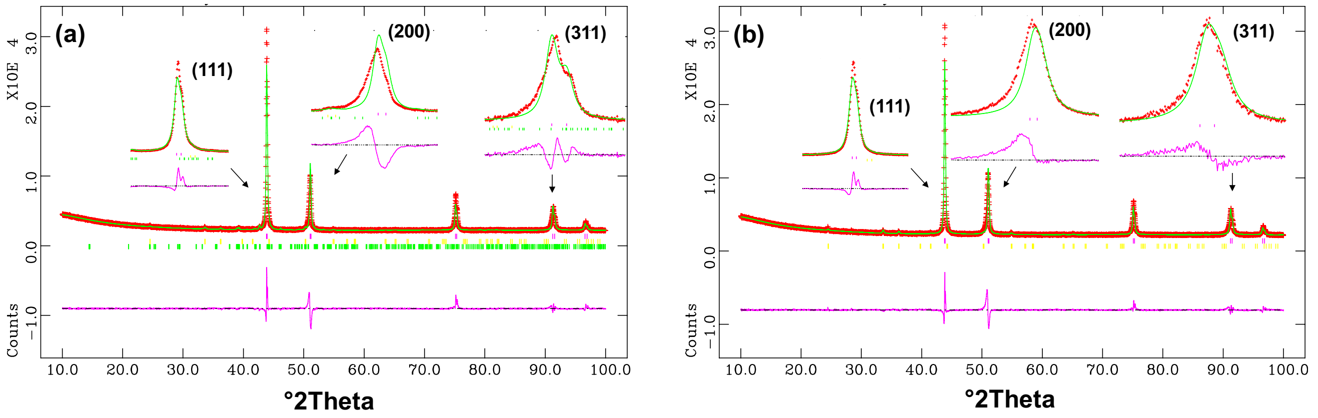

Fig. 15 The Rietveld refinement output of sintered CoCrFeNi obtained from powders admixed by mechanical mixing (**a**) and solvent-aided route (**b**). Data were collected in symmetric parallel beam configuration (X'Pert PRO diffractometer, PANalytical). The observed, calculated and difference curves are depicted. The vertical bars indicate the calculated positions of the Bragg reflections: (**a**) from the top: FCC phase, Cr_7C_3 (**b**) from the top: FCC phase, Cr_2O_3. The inserts in each figure show selected °2Theta ranges better elucidating the bad fits of reflection positions (discussed in the text)

(e.g., C_2H_4, C_2H_6), as reported by Zhang et al. [39]. Solid carbonaceous residues may also form. The presence of carbon-containing species (e.g., CO, CH_4, hydrocarbons, and residual carbon) may locally increase carbon activity within the compact during sintering and thereby promote chromium carbide formation (e.g., Cr_7C_3).

3.6.3 Lattice parameters and microstructure by XRPD

XRPD data collected in parallel beam configuration were elaborated by Rietveld refinements with the primary aim of determining the lattice constant of the FCC alloy, and consequently the real density used to determine the relative density (see Section 3.6.1). A *Fd*−3 *m* structure model was used assuming random site occupancies of the equimolar atoms. The experimental, fitted and difference curves are shown in Fig. 15. The refined average lattice constants were equal considering the error (3.57017 ± 0.00006 Å) for the mechanically admixed powder and 3.57004 ± 0.00007 Å for the powder admixed by the solvent-aided route. The corresponding densities were 8.228 g/cm^3 (mechanically mixed) and 8.229 g/cm^3 (solvent-aided route).

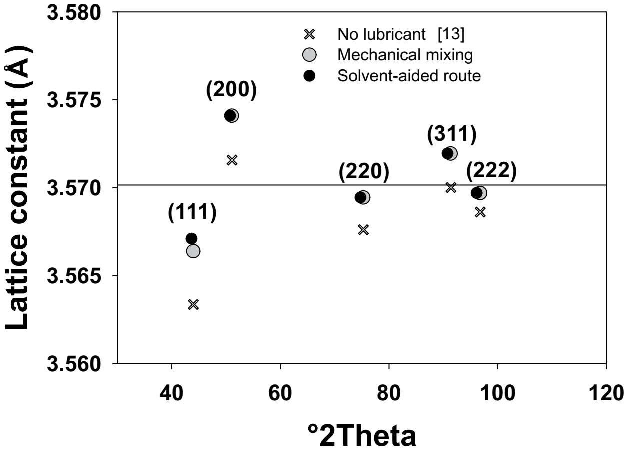

Fig. 16 Lattice constants derived separately from each Bragg reflection with Miller indices (hkl) (Rietveld refinements, symmetric parallel beam configuration for data collection). For comparison, data from previous work by Colombini et al. [13] are also shown. In that work, CoCrFeNi alloys were prepared using the same approach as in this work but without using a lubricant/binder during powder pressing. Errors are within symbols. The continuous line represents the "average" lattice constant obtained from Rietveld refinements

An interesting secondary observation can be made in Fig. 15. Whereas a good fit of the relative intensities is obtained, indicating random orientation of the crystallites, the positions of the reflections are not properly fitted (see difference curve in Fig. 15). This is particularly evident for the (111) and the (200) reflections (in opposite senses). The alloys thus present distorted unit cells. In addition, abnormal reflection shapes of the (200) and the (311) reflections are observed that could indicate direction-dependent strain (inserts in Fig. 15). In order to further evaluate the anisotropic characteristic of the alloys, the lattice constant was also calculated from each one of the five most intense Bragg reflections of the FCC phase. The results from these analyses are shown in Fig. 16 together with previously published data [13]. The continuous line indicates the "average" lattice parameter retrieved from Rietveld refinements. The line represents both of the investigated samples as the refined average lattice constants were equal considering the error (3.57017 ± 0.00006 Å for mechanical admixing and 3.57004 ± 0.00007 for the solvent-aided route). The distortion is manifested in variations in lattice constant depending on which Bragg reflection is considered. This type of deviation from an isotropic structure has been reported before for equimolar CoCrFeNi prepared by press-sinter processing [13] and arc-melting [56] as well as for arc-melted Pd-doped

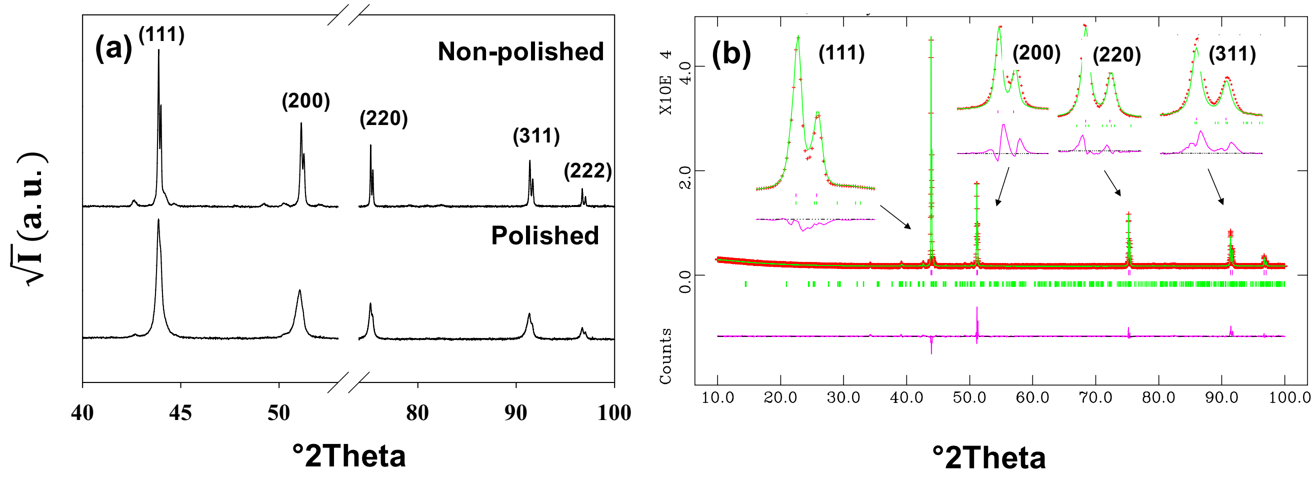

Fig. 17 XRPD data from a polished (lower) and non-polished (upper) sintered sample obtained from powder admixed using mechanical mixing (**a**). The results from Rietveld refinements using the isotropic FCC structure model and data collected from the non-polished sample (**b**). Note the perfect fit of the reflection positions with the isotropic FCC structure model (not obtained using data of polished sample, see Fig. 15a)

CoCrFeNi [57]. On the contrary, no deviation from the isotropic structure was found for atomized CoCrFeNi powders [8]. A plausible explanation to the observed reflection shifts, particularly evident for the (111) and (200) reflections, is strain anisotropies which manifest in direction-dependent changes in lattice constant with respect to the isotropic ideal structure [58]. Daymond et al. used neutron diffraction and Rietveld refinements to study the strain state of austenitic steel (pure FCC phase) under in situ loading [58]. The authors found that the elastic strain in different directions diverged with increasing load which led to shift of the reflection centers with respect to the isotropic structure model. In particular, the authors reported a negative shift of the (111) reflection and a positive one for the (200). This was indeed observed for the samples studied in this work and apparently also for the samples recently studied by Colombini et al. [13] (see Fig. 16). An explanation for the strain state of the FCC MPEA structure, is the standard mechanical chemical polishing procedure that was used to prepare the samples. Recently, nanoindentation measurements were performed on equimolar CoCrFeNi following differently prepared surfaces (standard chemical–mechanical polishing and electropolishing) [59]. The authors showed that a 11–17 um thick work hardened layer is formed following chemical–mechanical polishing, thus impairing a correct determination of the true materials' nanohardness. The plastically deformed layer is thus equal to or greater than the expected maximum penetration depth of the incidence Cu Kα X-ray beam (10.4 µm according to calculations using the X'Pert highscore plus software, PANalytical). Hence, both reflection broadening due to plastic deformation in the form of dislocations (microstrain) as well as anisotropically strained crystals (macrostrain) may be the result. To verify this assumption, XRPD data was collected from the as-sintered sample obtained from the powder admixed mechanically, i.e. without polishing. The results are shown in Fig. 17a. For comparison, data collected from the polished surface is also shown. Instead, Fig. 17b shows the results from the Rietveld refinement using the isotropic FCC structure model. Two important observations can be made: 1) the reflections in the pattern collected from the polished surface is much broader (Fig. 17a); 2) the positions of the reflections are perfectly fitted with the isotropic structure model for data collected on the non-polished sample (Fig. 17b). It can thus be concluded that standard metallographic polishing produces a damaged surface layer containing deformed crystallites (shift in reflection position, macrostrain) and microstrain (dislocations).

3.7 General discussion

The laser diffraction measurements showed very similar particle size distributions for the base powder and the powder admixed by the solvent-aided route (Fig. 4). Hence, the organic compound is likely distributed evenly on primary particles as observed by others [31]. Instead, the mechanical admixing leads to particle agglomeration (Figs. 4 and 5). In contrast to powders admixed by the solvent-aided route, mechanical mixing led to comminution of the particles (see Fig. 4) which most likely explains the higher density obtained after uniaxial pressing (Table 1). Particle fracturing during mechanical mixing is expected, as both ethanol and stearic acid are commonly used as process control agents (PCAs) in ball milling to limit cold welding and promote particle breakage and atomic mixing. While the resulting higher green density may be advantageous

(Table 1), particle rupture during admixing reduces process control and exposes fresh metal surfaces, increasing the risk of oxygen uptake. A major drawback of mechanical admixing is incomplete removal of the binder/lubricant, resulting in carbide formation during sintering (Fig. 10).

A major issue evidenced in both types of sintered samples is the presence of chromium oxides (Figs. 10, 13 and 14), already present in the pressed powders (see Figs. 7 and 8). This represents a limitation of the present processing conditions and may be mitigated by an appropriate sintering atmosphere. In fact, much work has been dedicated to the dissociation or reduction of oxides during sintering of e.g. steel alloyed with oxygen-sensitive elements such as chromium. Proper adjustment of the reduction potential of the sintering atmosphere is needed to reduce stable oxides on the powder surface and promote inter-particle bonding [60, 61]. It should be pointed out that the majority of the research work on PM processing of MPEAs deals with SPS of mechanically alloyed powders where carbide and oxide inclusions in the sintered material is often inevitable due to degradation of the organic PCA and contamination from the milling media (e.g. WC) [14, 53–55].

As a final remark, solvent-aided admixing of lubricant/binder warrants further systematic investigation. While mechanical admixing has been extensively optimized with respect to mixing time and powder properties to ensure e.g. steady die filling [30] and effective lubrication [33], the solvent-aided route has received considerably less attention from a process–performance perspective. In this approach, lubricant/binder deposition occurs through evaporative crystallization of the organic additive, making the final phase distribution highly sensitive to supersaturation conditions, evaporation rate, temperature, and stirring. Such parameters govern nucleation and growth phenomena, which ultimately determine how uniformly the lubricant/binder is distributed on particle surfaces. Previous studies have shown that crystallization behavior of stearic acid is strongly influenced by solvent type, cooling rate, temperature, and surfactant presence [62–64]. For example, the addition of Span-80 has been reported to slow stearic acid crystallization due to competitive interfacial adsorption [64]. Considering all these facts, it would be interesting to increase the knowledge on preparation procedure and correlate with processability in press-sinter operation, as already extensively done for mechanical mixing. The solvent-aided route may offer some important advantages from simple mixing in particular for irregular and fine powders with high internal friction like those used for reactive sintering starting from fine elemental powders. Further insights into these events and better control over process parameters could be beneficial for successive powder metallurgy processing of such powders. Nevertheless, the solvent-aided procedure adopted here proved suitable for press–sinter processing under the investigated conditions. Indeed, a FCC solid solution MPEA was obtained from compacts cold-pressed at relatively low pressure.

4 Conclusions

It was demonstrated that the low-pressure region of the compressibility curve (70–325 MPa), governed by densification by particle rearrangement, could be exploited for the synthesis of equimolar CoCrFeNi via cold uniaxial pressing and pressureless sintering. The application of this traditional forming method at low loads was made feasible by using admixed stearic acid, which attenuated wall and interparticle friction while simultaneously functioning as a binder. Special attention was given to the lubricant/binder admixing method, comparing solvent-aided and mechanical mixing routes. The results show that the two approaches lead to distinct process–structure relationships. Mechanical admixing promotes particle comminution and higher green density, but also results in the formation of binder-rich agglomerates and incomplete debinding, leading to carbide formation after sintering. In contrast, the solvent-aided route preserves the particle size distribution and enables a more uniform distribution of the organic additive on particle surfaces, facilitating binder removal and limiting carbon-related contamination, albeit at the expense of lower densification. Reactive sintering of the fine elemental powders at 1200 °C resulted in the formation of a face-centered cubic CoCrFeNi multi-principal element alloy. The present results demonstrate the feasibility of combining low-pressure forming with binder-assisted compaction and reactive sintering for the processing of fine, poorly compactable powders. The proposed approach provides a simplified processing route for MPEAs from fine elemental powders, particularly relevant for applications such as sputtering targets for physical vapor deposition (PVD), where compositional control is more critical than full densification. Finally, the results highlight the persistent challenge of oxide formation during powder metallurgy processing of MPEAs, even under controlled atmospheres. Further optimization of sintering conditions, including the use of reducing atmospheres, is required to mitigate oxide formation and improve material quality. At the same time, for sputtering-target applications, the presence of oxygen-bearing phases may also open interesting perspectives for the synthesis of oxide-dispersion-strengthened (ODS)-like coatings [22], an aspect that deserves dedicated investigation in future work.

Supplementary Information The online version contains supplementary material available at https://doi.org/10.1007/s00170-026-18155-w.

Acknowledgements The authors kindly thank Fernanda Andreola (University of Modena and Reggio Emilia, Italy) for performing the mercury intrusion experiments.

Author contribution The study was conceived and designed by M. Lassinantti Gualtieri together with the co-authors. Material preparation, data collection, and analysis were mainly carried out by M. Lassinantti Gualtieri with input and contributions from E. Paradisi, E. Colombini and C. Mortalò. All authors contributed to the interpretation of the results and critical revision of the manuscript. The study was supervised by P. Veronesi. All authors approved the final version of the manuscript.

Funding Open access funding provided by Università degli Studi di Modena e Reggio Emilia within the CRUI-CARE Agreement. The authors declare that no funds, grants, or other support were received during the preparation of this manuscript.

Declarations

Competing interests The authors have no relevant financial or non-financial interests to disclose.

References

1. Miracle DB, Senkov ON (2017) A critical review of high entropy alloys and related concepts. Acta Mater 122:448. https://doi.org/10.1016/j.actamat.2016.08.081
2. Yeh J-W, Chen S-K, Lin S-J, Gan J-Y, Chin T-S, Shun T-T, Tsau C-H, Chang S-Y (2004) Nanostructured high-entropy alloys with multiple principal elements: novel alloy design concepts and outcomes. Adv Eng Mater 6:299. https://doi.org/10.1002/adem.200300567
3. Cantor B (2024) Exploring multicomponent phase space to discover new materials. J Phase Equilib Diffus 45:188–218. https://doi.org/10.1007/s11669-024-01131-w
4. Filho FDC, Ritchie RO, Meyers MA, Monteiro SN (2022) Cantor-derived medium-entropy alloys: bridging the gap between traditional metallic and high-entropy alloys. J Mater Res Technol 17:1868. https://doi.org/10.1016/j.jmrt.2022.01.118
5. Wu Z, Bei H, Pharr GM, George EP (2014) Temperature dependence of the mechanical properties of equiatomic solid solution alloys with face-centered cubic crystal structures. Acta Mater 81:428. https://doi.org/10.1016/j.actamat.2014.08.026
6. Wang J, Yu Y, Yu Y, Zhao Y, Zhang Y, Han X (2020) Comparison of the corrosion and passivity behavior between CrMnFeCoNi and CrFeCoNi coatings prepared by argon arc cladding. J Mater Res Technol 9:8482. https://doi.org/10.1016/j.jmrt.2020.05.093
7. Chen X, Qin G, Gao X, Chen R, Song Q, Cui H (2023) Strengthening CoCrFeNi high entropy alloy by in-situ phases of Laves and ZrC. Met Mater Int 29:1390. https://doi.org/10.1007/s12540-022-01314-5
8. Liu WH, Lu ZP, He JY, Luan JH, Wang ZJ, Liu B, Liu Y, Chen MW, Liu CT (2016) Ductile CoCrFeNiMox high entropy alloys strengthened by hard intermetallic phases. Acta Mater 116:332. https://doi.org/10.1016/j.actamat.2016.06.063
9. Praveen S, Basu J, Kashyap S, Kottada R (2016) Exceptional resistance to grain growth in nanocrystalline CoCrFeNi high entropy alloy at high homologous temperatures. J Alloys Compd 662:361. https://doi.org/10.1016/j.jallcom.2015.12.020
10. Lone NF, Czerwinski F, Chen D (2024) Present challenges in development of lightweight high entropy alloys: a review. Appl Mater Today 39:102296. https://doi.org/10.1016/j.apmt.2024.102296
11. Zhang W, Chabok A, Kooi BJ, Peni Y (2022) Additive manufactured high entropy alloys: a review of the microstructure and properties. Mater Des 220:110875. https://doi.org/10.1016/j.matdes.2022.110875
12. ISO (2023) Powder metallurgy—Vocabulary (ISO 3252). ISO
13. Colombini E, Lassinantti Gualtieri M, Mortalò C, Deambrosis SM, Montagner F, Zin V, Miorin E, Valsecchi G, Fabrizio M, Veronesi P (2022) Powder metallurgy route for the synthesis of multiprincipal element alloys sputtering targets. Adv Eng Mater 24:2101518. https://doi.org/10.1002/adem.202101518
14. Bijjala ST, Wilkerson R, Beamer C, Kumar P (2024) Understanding the phase evolution and elemental distribution in MoWTaNbVTix manufactured via powder metallurgical approach. Int J Adv Manuf Technol 135:5925–5943. https://doi.org/10.1007/s00170-024-14856-2
15. Meza A, Barbosa A, Tabares E, Torralba JM (2024) Tailoring high-entropy alloys via commodity powders for metal injection moulding: a feasibility study. J Mater Res Technol 31:109–116. https://doi.org/10.1016/j.jmrt.2024.06.034
16. Pan X, Wang X, Qui C (2024) Microstructural development and mechanical behavior of a near-eutectic high entropy alloy Al1.8CrCuFeNi2 fabricated by hot isostatic pressing. Intermetallics 171:108361. https://doi.org/10.1016/j.intermet.2024.108361
17. Martin P, Aguilar C, Cabrera JM (2024) A review on mechanical alloying and spark plasma sintering of refractory high-entropy alloys: challenges, microstructures, and mechanical behavior. J Mater Res Technol 30:1900–1928. https://doi.org/10.1016/j.jmrt.2024.03.205
18. Olorundaisi E, Babalola BJ, Bayode BL, Teffo L, Olubambi PA (2023) Optimization of process parameters for the development of Ni–Al-Ti-Mn-Co-Fe–Cr high entropy alloy system via spark plasma sintering. Int J Adv Manuf Technol 126:3323–3337. https://doi.org/10.1007/s00170-023-11311-6
19. Moazzen P, Toroghinejad M, Aghayar Y, Zargar T, Davoodi F, Mohammadi M (2024) Exploring nanocrystalline high entropy alloys fabricated via mechanical alloying (MA) and spark plasma sintering (SPS): a review. High Entropy Alloys & Materials 2:175–218. https://doi.org/10.1007/s44210-024-00038-y
20. Kumar S (2024) <article-title update="added">Comprehensive review on high entropy alloy-based coating. Surf Coat Technol 477:130327. https://doi.org/10.1016/j.surfcoat.2023.130327
21. Li W, Liu P, Liaw PK (2018) Microstructures and properties of high-entropy alloy films and coatings: a review. Mater Res Lett 6:199–229. https://doi.org/10.1080/21663831.2018.1434248
22. Lee S, Chatain D, Liebscher CH, Dehm G (2021) Structure and hardness of in situ synthesized nano-oxide strengthened CoCrFeNi

high entropy alloy thin films. Scripta Mater 203:114044. https://doi.org/10.1016/j.scriptamat.2021.114044
23. Simchi A (2003) Effects of lubrication procedure on the consolidation, sintering and microstructural features of powder compacts. Mater Des 24:585. https://doi.org/10.1016/S0261-3069(03)00155-9
24. Ward M, Billington JC (1979) Effect of zinc stearate on apparent density, mixing, and compaction/ejection of iron powder compacts. Powder Metall 4:201. https://doi.org/10.1179/pom.1979.22.4.20
25. Fogagnolo JB, Ruiz-Navas EM, Robert MH, Torralba JM (2003) The effects of mechanical alloying on the compressibility of aluminium matrix composite powder. Mater Sci Eng A 355:50. https://doi.org/10.1016/S0921-5093(03)00057-1
26. Sivasankaran S, Al-Mufadi FA, Ammar HR (2021) Influence of V and Zn in FeCrCuMnTi high-entropy alloys on microstructures and uniaxial compaction behavior prepared by mechanical alloying. Crystals 11:1413. https://doi.org/10.3390/cryst11111413
27. Kozub B, Uthayakumar M, Kazor J (2022) The influence of nanographite addition on the compaction process and properties of AISI 316L sintered stainless steel. Materials 15:3629. https://doi.org/10.3390/ma15103629
28. Zhang X, Huang Y, Liu X, Yang L, Shi C, Wu Y, Tang W (2018) Microstructures and properties of 40Cu/Ag(Invar) composites fabricated by powder metallurgy and subsequent thermo-mechanical treatment. Metall Mater Trans A 49:1869. https://doi.org/10.1007/s11661-018-4548-9
29. Ghasemi S, Azadbeh M, Mousapour M, Mohammadzadeh A, Danninger H, Salimi N (2020) The role of pore evolution during supersolidus liquid phase sintering of prealloyed brass powder. Powder Metall 63:187. https://doi.org/10.1080/00325899.2020.1785155
30. Nijikovsky B, Aguirre Perales L, Brika SE, Brailovski V (2020) Towards reliable optimization of metal powder–lubricant mixing for high die filling performance: exploring a rheology based approach. Powder Technol 362:168. https://doi.org/10.1016/j.powtec.2019.12.003
31. Chen W, Wang J, Wang S, Chen P, Cheng J (2020) On the processing properties and friction behaviours during compaction of powder mixtures. Mater Sci Technol 36:1057. https://doi.org/10.1080/02670836.2020.1747779
32. Liu Z, Li H, Liu X, Li D, Huang Z, Fang Z, Zou Y (2019) Effect of warm compaction lubricant on the properties of Fe-based powder metallurgy materials. Mater Res Express 6:046534. https://doi.org/10.1088/2053-1591/aafbfa
33. Ward M (1979) Influence of lubricants on dimensional changes and mechanical properties of sintered ferrous compacts. Powder Metall 22:193. https://doi.org/10.1179/pom.1979.22.4.193
34. Chen Y, Zhang L, Sun H, Chen F, Qu X (2020) Design of the thixotropic lubricant and its influence on compaction behavior of Cr-alloyed PM steel. Metal Powder Rep 75:142. https://doi.org/10.1016/j.mprp.2019.04.062
35. Korim NS, Elsayed A, Hu L (2022) Impacts of lubricant type on the densification behavior and final powder compact properties of Cu–Fe alloy under different compaction pressures. Materials 15:5750. https://doi.org/10.3390/ma15165750
36. Heryanto R, Hasan M, Abdullah EC, Kumoro AC (2007) Solubility of stearic acid in various organic solvents and its prediction using non-ideal solution models. ScienceAsia 33:469. https://doi.org/10.2306/scienceasia1513-1874.2007.33.469
37. Garti N, Sarig S, Wellner E (1980) Determination of the composition of mixtures of fatty acid polymorphs by DTA. Thermochim Acta 37:131–136. https://doi.org/10.1016/0040-6031(80)80033-5
38. Lerdkanchanaporn S, Dollimore D (1998) An investigation of the evaporation of stearic acid using a simultaneous TG-DTA unit. Thermochim Acta 324:15–23. https://doi.org/10.1016/S0040-6031(98)00519-X
39. Zhang Y, Zhang C, Li W, Xiao Q, Jiao F, Xu S, Lan Y, Fu Y, Shu C-M, Cao W (2023) Reaction mechanism of stearic acid pyrolysis via reactive molecular dynamics simulation and TG-IR technology. Renew Energy 217:119115. https://doi.org/10.1016/j.renene.2023.119115
40. Shu C, Yao Z, Li X, Du W, Tao Z, Yang H (2022) Microstructure and wear mechanism of CoCrCuFeNiVx high entropy alloy by sintering and electron beam remelting. Physica B 638:413834. https://doi.org/10.1016/j.physb.2022.413834
41. Carr RL (1965) Evaluating flow properties of solids. Chem Eng 72:163–168
42. Larson AC, Von Dreele RB (1994) Generalized structure analysis system (GSAS). Natl Lab Rep LAUR 86–748, Los Alamos
43. Toby BH (2001) EXPGUI, a graphical user interface for GSAS. J Appl Crystallogr 34:210. https://doi.org/10.1107/S0021889801002242
44. Gražulis S, Chateigner D, Downs RT, Yokochi AFT, Quirós M, Lutterotti L, Manakova E, Butkus J, Moeck P, Le Bail A (2009) Crystallography open database–an open-access collection of crystal structures. J Appl Crystallogr 42:726. https://doi.org/10.1107/S0021889809016690
45. Washburn EW (1921) The dynamics of capillary flow. Phys Rev 17:273. https://doi.org/10.1103/PhysRev.17.273
46. Sivasankaran S, Sivaprasad K, Narayanasamy R, Iyer VK (2010) An investigation on flowability and compressibility of AA 6061–100−x–x wt.% TiO2 micro and nanocomposite powder prepared by blending and mechanical alloying. Powder Technol 201:70. https://doi.org/10.1016/j.powtec.2010.03.013
47. Yim D, Jang MJ, Bae JW, Moon J, Lee C-H, Hong S-J, Hong SI, Kim HS (2018) Compaction behavior of water-atomized CoCrFeMnNi high-entropy alloy powders. Mater Chem Phys 210:95. https://doi.org/10.1016/j.matchemphys.2017.06.013
48. Sarwat SG (2017) Contamination in wet-ball milling. Powder Metall 60:267. https://doi.org/10.1080/00325899.2017.128064
49. Rangel RL, Kisuka F, Hare C, Vivacqua V, Franci A, Oñate E, Wu C-Y (2023) Experimental investigation of heat generation during granular flow in a rotating drum using infrared thermography. Powder Technol 426:118619. https://doi.org/10.1016/j.powtec.2023.118619
50. Collins TJ (2007) ImageJ for microscopy. Biotechniques 43:25. https://doi.org/10.2144/000112517
51. Li Y, Liu S, Qu X, Huang B (2003) Thermal debinding processing of 316L stainless steel. J Mater Process Technol 137:65. https://doi.org/10.1016/S0924-0136(02)01067-1
52. Fourmont A, Gallet SL, Hoummada K, Descoins M, Desgranges C, Politano O, Baras F (2021) Effects of mechanical activation on chemical homogeneity and contamination level in dual-phase AlCoCrFeNi high entropy alloy. Mater Chem Phys 272:125000. https://doi.org/10.1016/j.matchemphys.2021.125000
53. Li M, Guo Y, Wang H, Shan J, Chang Y (2020) Microstructures and mechanical properties of oxide dispersion strengthened CoCrFeNi high-entropy alloy produced by mechanical alloying and spark plasma sintering. Intermetallics 123:106819. https://doi.org/10.1016/j.intermet.2020.106819
54. Garlapati MM, Vaidya M, Karati A, Mishra S, Bhattacharya R, Murty BS (2020) Influence of Al content on thermal stability of nanocrystalline AlxCoCrFeNi high entropy alloys at low and intermediate temperatures. Adv Powder Technol 31:1985. https://doi.org/10.1016/j.apt.2020.02.032
55. Veronesi P, Lassinantti Gualtieri M, Feltrin AC, Akhtar F, Colombini E (2023) Recycling of spent powders from additive manufacturing processing of Inconel 625 for the synthesis of CoCrFeNiMoxNb0.4x (x = 0–0.1) multi-principal element alloys (MPEAs) by spark plasma sintering (SPS) of mechanically

alloyed powders. In: Euro powder metallurgy 2023 congress and exhibition, PM 2023. European Powder Metallurgy Association (EPMA), 2023. https://doi.org/10.59499/EP235765342

56. Dahlborg U, Cornide J, Calvo-Dahlborg M, Hansen TC, Fitsch A, Leong Z, Chambreland S, Goodall R (2016) Structure of some CoCrFeNi and CoCrFeNiPd multicomponent HEA alloys by diffraction techniques. J Alloys Compd 681:330. https://doi.org/10.1016/j.jallcom.2016.04.248
57. Zhang F, Tong Y, Jin K, Bei H, Weber WJ, Zhang Y (2018) Lattice distortion and phase stability of Pd-doped NiCoFeCr solid-solution alloys. Entropy 20:900. https://doi.org/10.3390/e20120900
58. Daymond MR, Bourke MAM, Von Dreele RB, Clausen B, Lorentzen T (1997) Use of rietveld refinement for elastic macrostrain determination and for evaluation of plastic strain history from diffraction spectra. J Appl Phys 82:1554. https://doi.org/10.1063/1.365956
59. Lassinantti Gualtieri M, Colombini E, Testa V, Bolelli G, Giovanardi R, Veronesi P (2023) High-throughput nanoindentation mapping of a microsegregated CoCrFeNi multi-principal element alloy (MPEA): challenges and limitations. Adv Eng Mater 25:2300110. https://doi.org/10.1002/adem.202300110
60. de Oro Calron R, Gierl-Mayer C, Danninger H (2017) Master alloys in powder metallurgy: the challenge of exploring new alloying compositions. Powder Metall 60:86. https://doi.org/10.1080/00325899.2016.1269430
61. Hryha E, Dudrova E, Nyborg L (2012) On-line control of processing atmospheres for proper sintering of oxidation-sensitive PM steels. J Mater Process Technol 212:977. https://doi.org/10.1016/j.jmatprotec.2011.12.008
62. Sato K, Boistelle R (1984) Stability and occurrence of polymorphic modifications of stearic acid in polar and nonpolar solutions. J Cryst Growth 66:441. https://doi.org/10.1016/0022-0248(84)90228-8
63. Garti N, Wellner E, Sarig S (1981) Effect of food emulsifiers on crystal structure and habit of stearic acid. JAOCS 58:1050. https://doi.org/10.1007/BF02679326
64. Goswami H, Seth JR (2019) Influence of surfactant on crystallization kinetics of stearic acid. Ind Eng Chem Res 58:7661. https://doi.org/10.1021/acs.iecr.8b05954